PHYSIOGRAPHIC MAP OF WESTERN OREGON

Map labels:

N

Coast Range

Willamette Lowland

Cascade Volcanic Arc

Klamath Mountains

Cascadia — — Subduction — — Zone

0 — 75 km

Handwritten annotations:

Lump Sum

Contractor
Design — Build

Contractor
Takes Risk

ODOT
Design — Bid — Build

ODOT
Takes Risk

Large Scale
Landslides

Landslides
up to 70 Toot
Several 1000 ft long

Budget
Overruns

Biggest
Expensive

Highway
Construction =
Economic Stimulus
Climate Construction =
Watsonville, CA
Joe Savine —
Dec. 2006

Hwy 20
High Fatality
Rate

Factor of
Safety
Ø = internal Φ
friction
S.F. > 1.0 =
Slide prone
Ø = 12°

Legend:

Oregon Coast Range

Unglaciated, forested landscape

Paleogene-Neogene marine volcanic and sedimentary rocks (Walker and MacLeod, 1991)

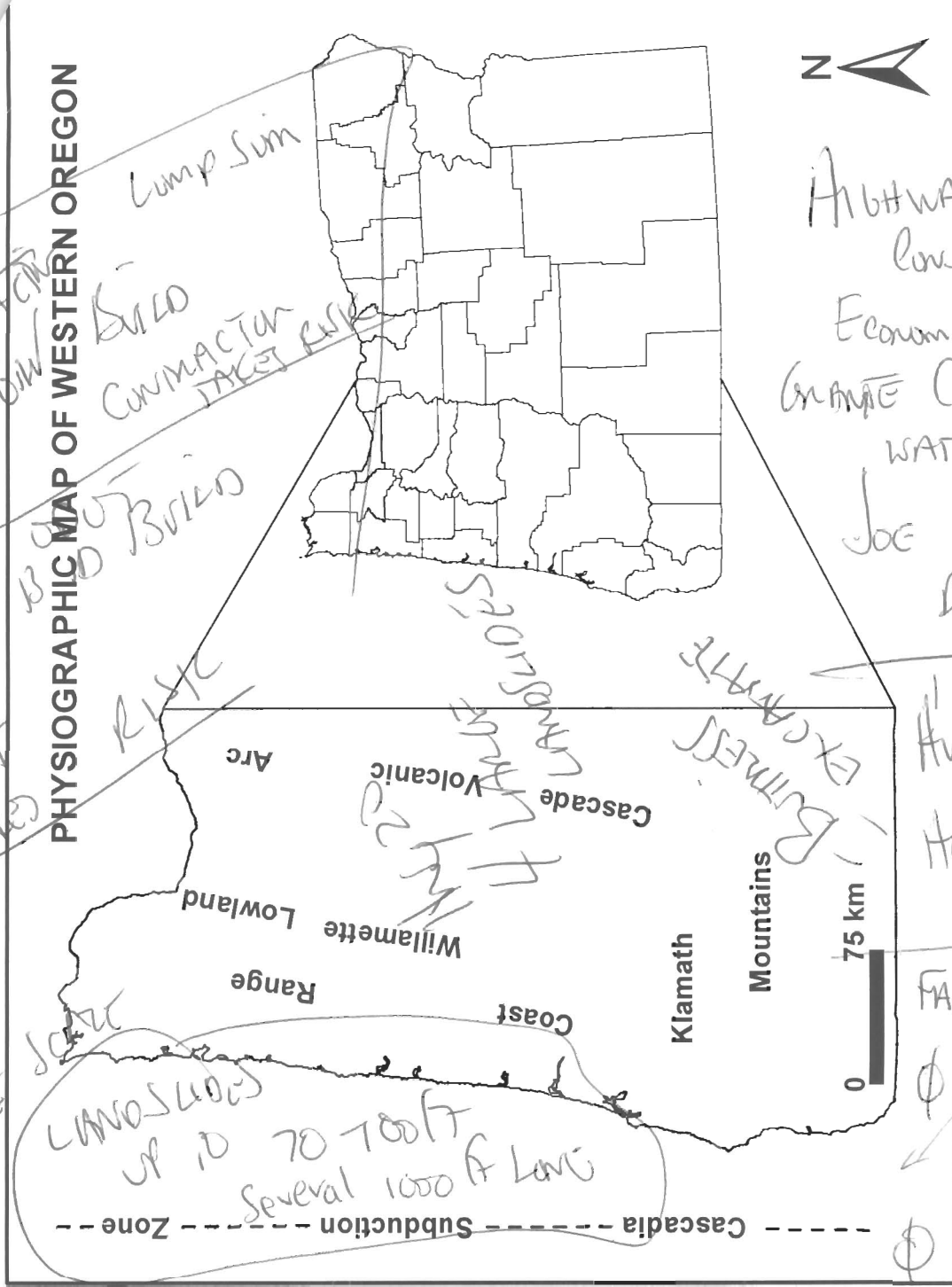Long history of oblique convergence and tectonic accretion (Wells et al., 1984)

Active mountain building during the past 10-15 Ma (Snavely et al., 1993)

Pleistocene uplift rates = 0.1-0.3 mm/yr (Kelsey et al., 1996)

Historic uplift rates = 1-3 mm/yr (Mitchell et al., 1994)

Eastward tilting = 1×10^{-8} rad/yr (Adams, 1984)

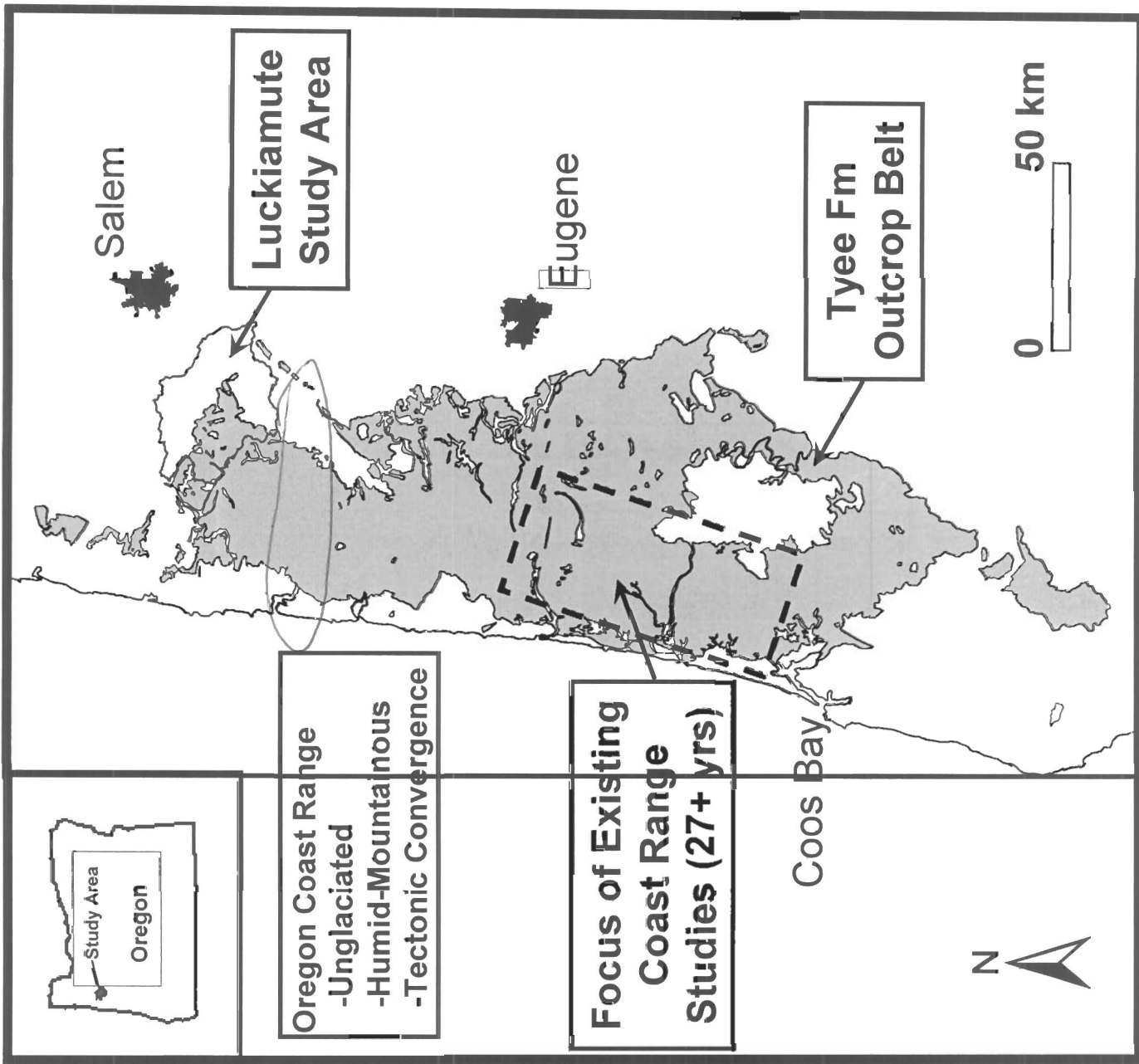Holocene erosion rates = 0.05-0.33 mm/yr (Roering et al., 2005)
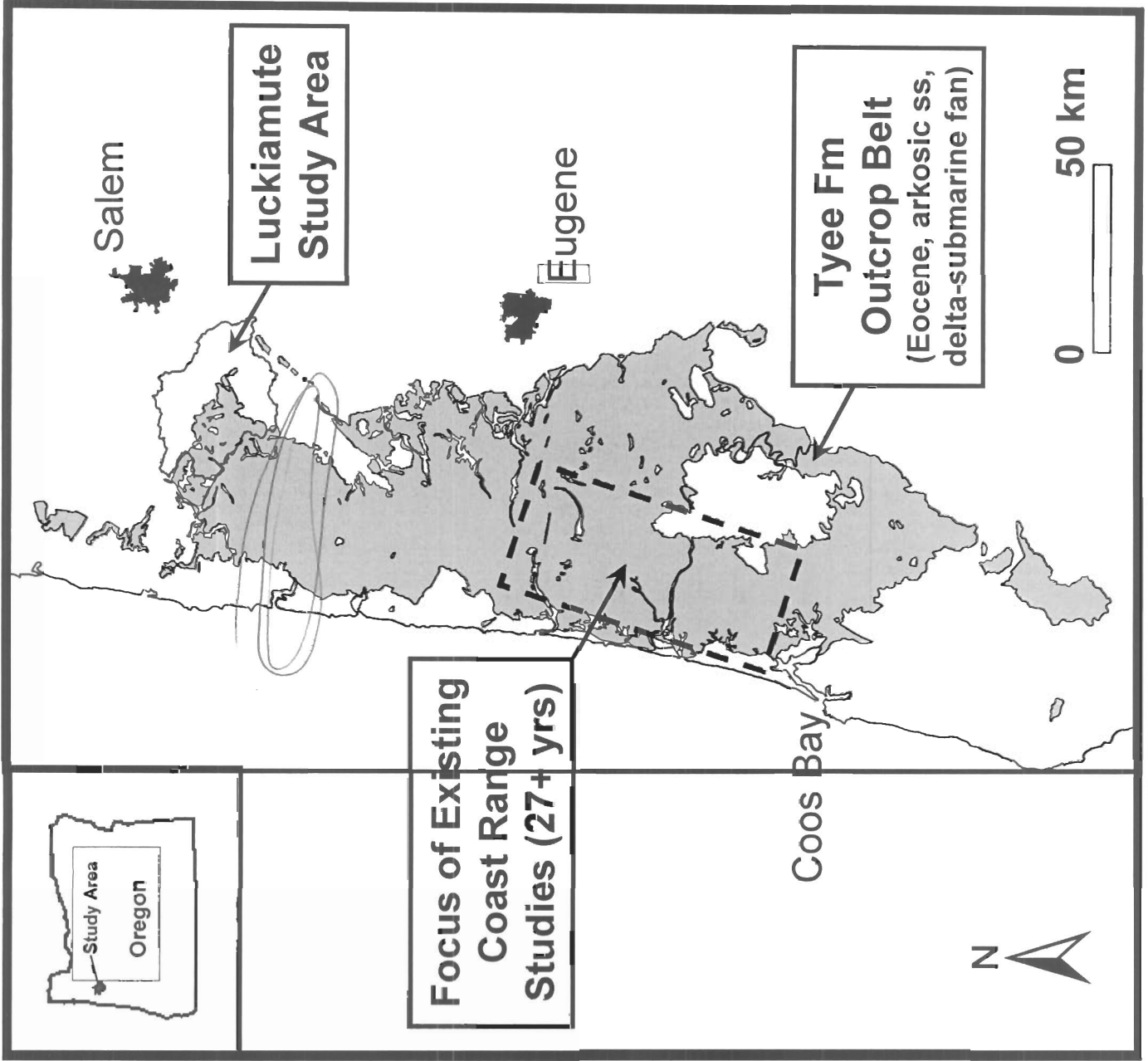
Salem

Luckiamute Study Area

Eugene

Tyee Fm Outcrop Belt

Oregon Coast Range
-Unglaciated
-Humid-Mountainous
-Tectonic Convergence

Focus of Existing Coast Range Studies (27+ yrs)

Coos Bay

Study Area

Oregon

0   50 km

N

3

Salem

Luckiamute
Study Area

Eugene

Tyee Fm
Outcrop Belt
(Eocene, arkosic ss,
delta-submarine fan)

0   50 km

Focus of Existing
Coast Range
Studies (27+ yrs)

Coos Bay

N

Study Area
Oregon
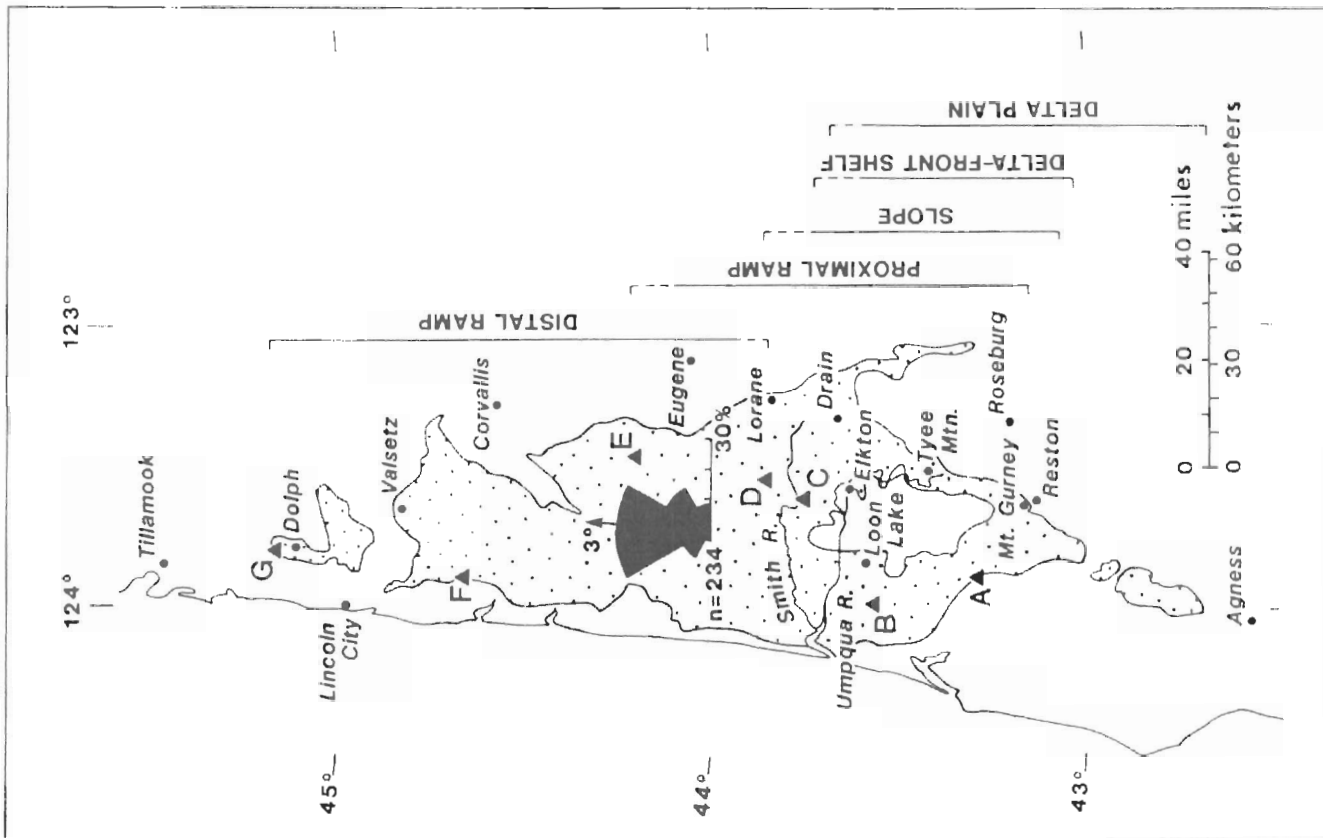
4

Paleocurrent analysis of Tyee-domain (from Heller and Dickinson, 1985)

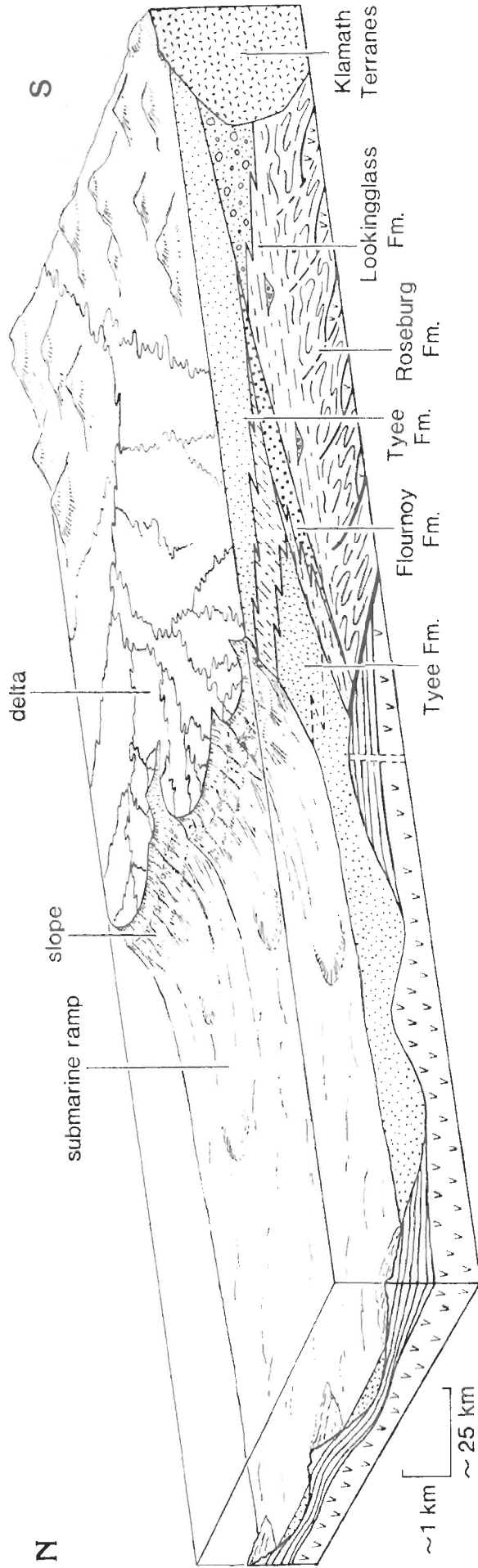# Paleogeographic reconstructions of Tyee-domain (from Heller and Dickinson, 1985)

Figure 8—Paleogeographic reconstruction of southern part of Oregon Coast Range during Eocene deposition of Tyee Formation (cf. Chan and Dott, 1983). See Figure 9 for actual (measured) facies relations within Tyee Formation.

Stratigraphic correlation chart of Tyee-domain (from Heller and Dickinson, 1985)
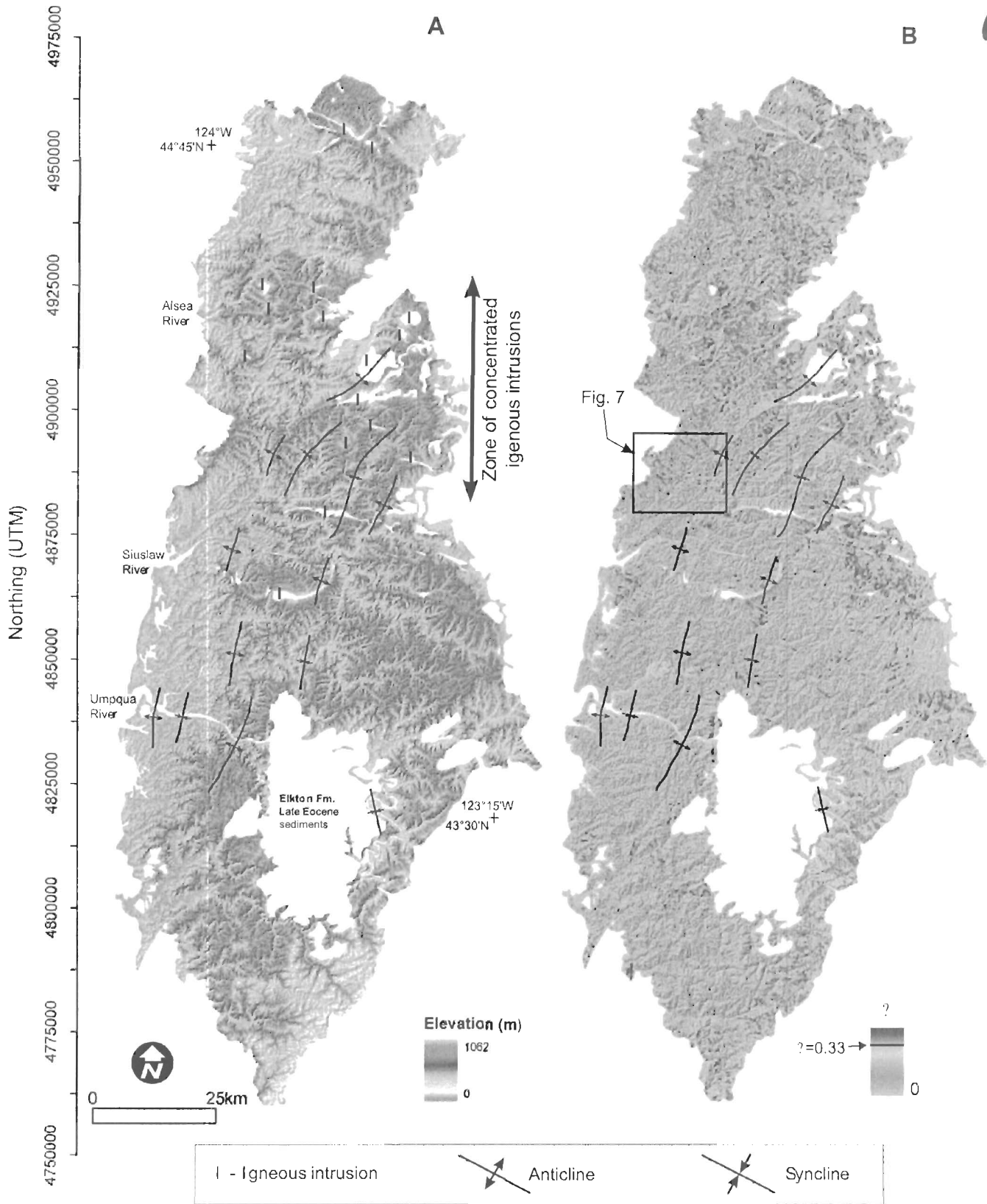
6
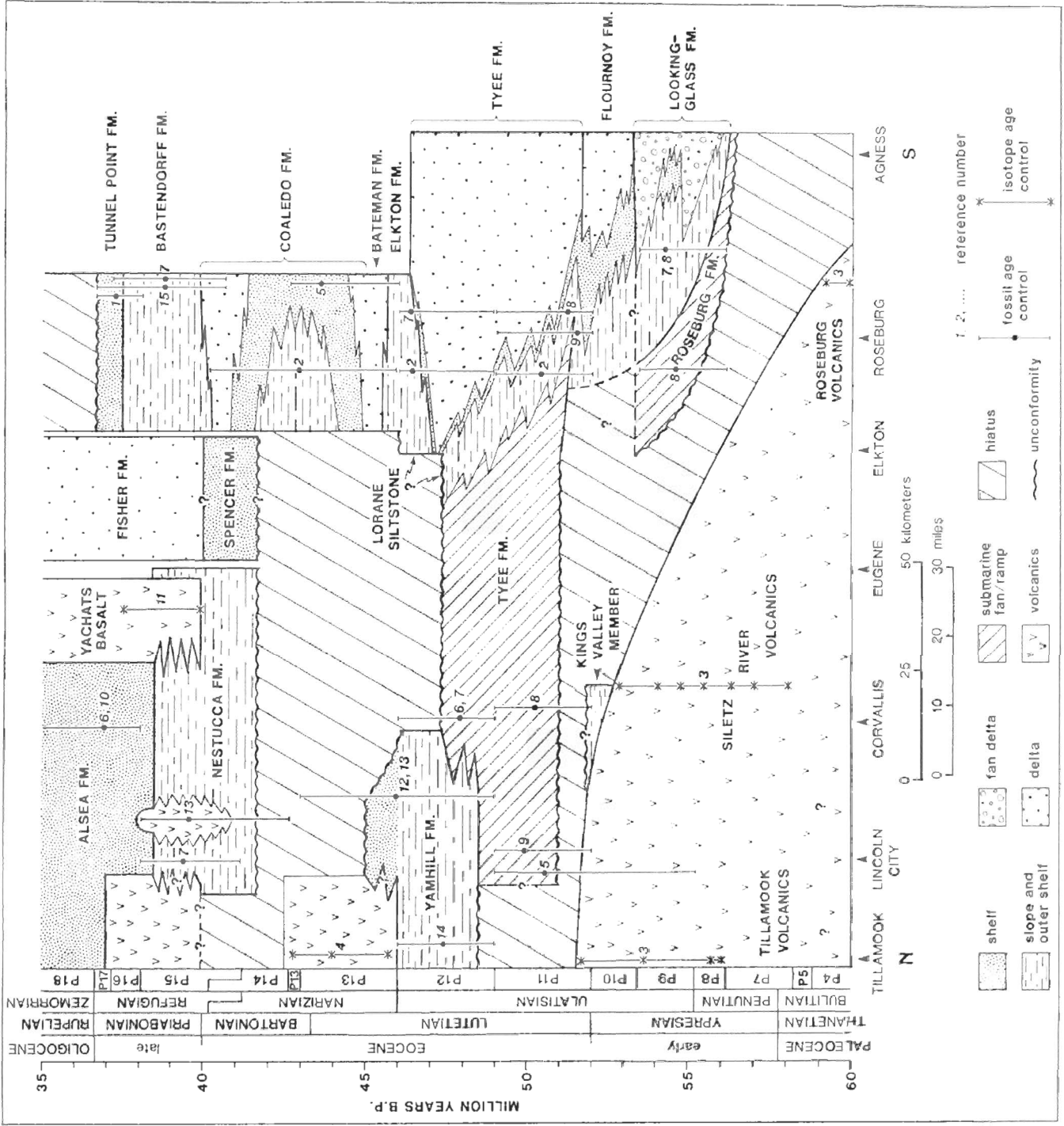
7

Figure 2. Elevation and deep-seated landslide terrain in the Tyee Formation. (A) Elevation with mapped distribution of anticlines and synclines (Baldwin, 1956, 1959, 1961). (B) Distribution of β values that quantify the degree to which terrain exhibits the topographic signature of deep-seated landsliding (see text). β varies from 0 to 1; 0 corresponds to steep and dissected terrain without indication of deep-seated landsliding and 1 represents terrain with morphology consistent with that generated by deep-seated landslides. On the basis of field observations and air photo analysis, β = 0.33 (which corresponds to the transition from burnt yellow to red) suitably demarcates boundaries of slide masses. In the southern interior, a patch of highly indurated, late Eocene sediments of the Elkton Formation occur and tend to form steep bedrock cliffs that contrast with the topography of the Tyee units.

Figure 3. Oblique photos of (A) steep and dissected terrain often cited as characteristic of the Oregon Coast Range (OCR), and (B) an ancient deep-seated landslide in the OCR (latitude: 43.47°N, longitude: 124.12°W) that exhibits a low-gradient, benchlike morphology.

generally, the role of deep-seated landsliding in regulating sediment production and landscape morphology is poorly understood.

TOPOGRAPHIC IDENTIFICATION AND MAPPING OF DEEP-SEATED LANDSLIDES

Here, we exploit the profound morphologic manifestation of deep-seated landslides in the OCR to automatically map their extent using a digital elevation model (DEM). Figure illustrates an east-west–trending ridge line with characteristic forms on either side; the north-facing flank of the ridge is distinguished by steep and dissected terrain whereas the southern flank exhibits a benchlike, low-gradient form. On the northern side, the integrated valley network facilitates the delivery of sediment from hillslopes and topographic hollows to higher-order channels via debris flows (Dietrich and Dunne, 1978; Benda and Dunne, 1997). In contrast, the poorly dissected slopes on the southern side arise from deep-seated slope instability that occurs frequently enough to suppress the development of valley networks (Fig. 5). No historical deformation has occurred at this site, but degraded headscarps similar to those shown in Figure 3B attest to the history of slope deformation. Along the base of the ancient landslide, valley incision has steepened slopes at the channel margin. Similarly steep sections were commonly observed during our field investigations of over 40 ancient deep-seated landslides in the OCR. Typically, dormant landslides exhibit: (1) >10-m-high, degraded headscarps, (2) low-gradient, hummocky benches with poorly developed drainage, and (3) steep lower slopes with active streamside soil slips. At some sites, the steep, lower slope segment, which may reflect the legacy of valley incision (Kelsey, 1988; Densmore and Hovius, 2000), was poorly developed or absent.

Method

The topographic signature of deep-seated slope failure is immediately apparent via inspection of aerial photos and topographic maps. To streamline the mapping process, we formulated a quantitative method for delineating landslide-dominated terrain from DEM data. For this endeavor, we acquired a DEM of the Oregon Coast Range from the USGS National Elevation Data set (NED), which has a grid spacing of ~26.5 m and boasts minimal edge matching and other artifacts. We compared the data against available 10 m DEMs and concluded that the 26.5 m data set was sufficient for distinguishing the topographic signature of deep-seated land-
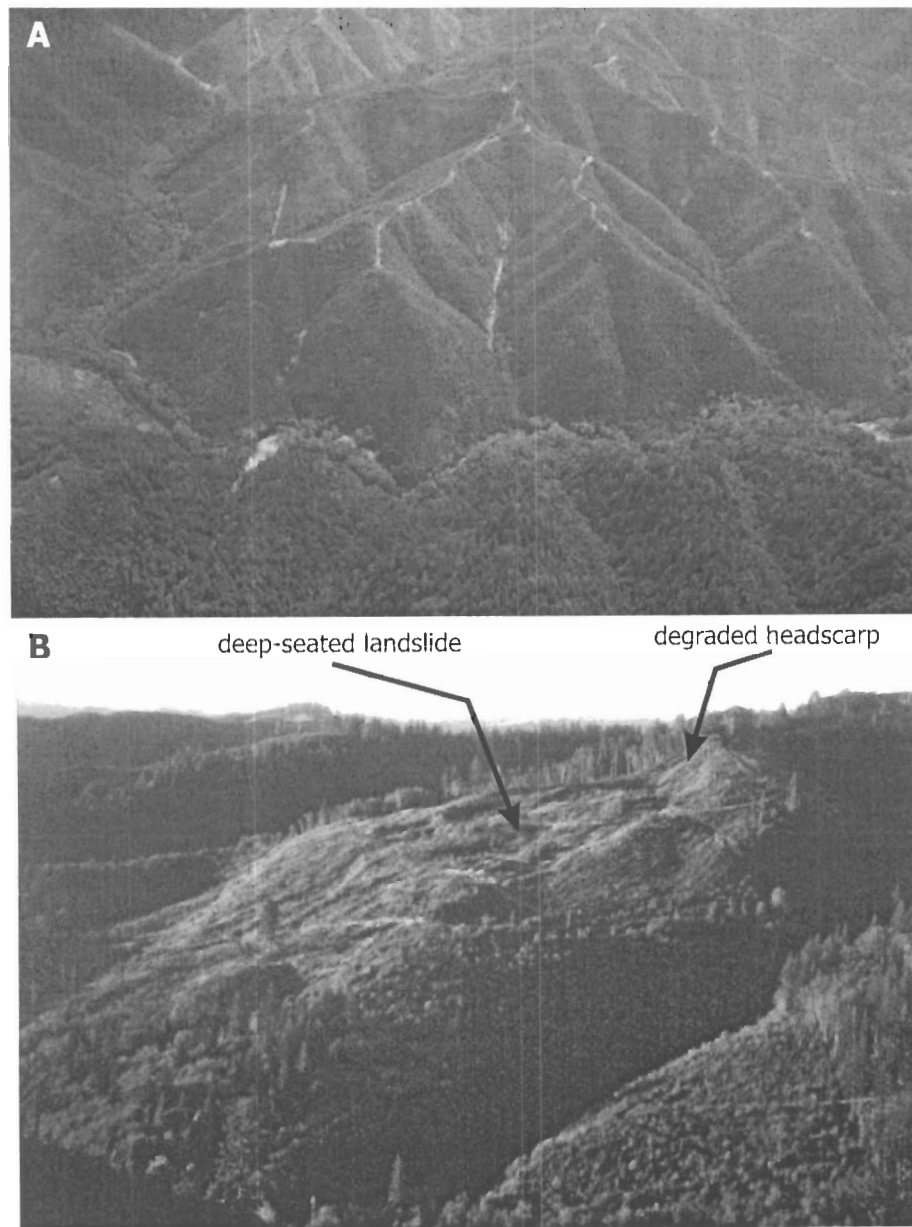
ROERING et al.

sliding and allowed for faster computational time. Using a digital database derived from the Oregon State geological map (Walker and MacLeod, 1991), we clipped topography from the DEM with a digital coverage outlining the extent of the Tyee Formation (see Fig. 2A). Small voids in the clipped topography (shown with the letter "I" superimposed) represent igneous intrusive rocks that are more resistant to erosion than the Tyee Formation and tend to be associated with large knickpoints in river profiles.

We used topographic maps, aerial photos, and field observations to identify and map several ridges that exhibit both steep and dissected terrain and deep-seated landslide-prone terrain (see Fig. 5). Reasoning that the morphologic differences that distinguish the two process domains may be reflected by their slope and degree of curvature, we calculated the distribution of topographic derivatives gradient ($|\nabla z|$) and curvature (estimated here as the Laplacian operator, $\nabla^2 z$) for both sides of each ridge using algorithms summarized by Zevenbergen and Thorne (1987) and Moore et al. (1991). Positive values of curvature reflect concave terrain such as that associated with unchanneled valleys or hollows, whereas negative values represent convex forms such as hilltops. We plotted the variation of curvature with gradient for steep and dissected terrain, deep-seated landslide terrain, and nearby valley floors (two examples are shown in Fig. 6). With minimal overlap, each landform type exhibits its own morphologic signature in gradient-curvature space. We defined the range of gradient and curvature values that best distinguishes the cluster of points associated with deep-seated landslides. For various combinations of gradient and curvature values, we calculated the fraction of deep-seated, valley floor, and steep/dissected data that fall within the topographic envelope. To determine the best-fit envelope, we simultaneously maximized the fraction of deep-seated data and minimized the fraction of valley floor and steep/dissected data that plot within the topographic envelope. The calibrated morphologic envelope indicates that deep-seated landslides (filled circles on Fig. 6) are distinguished by near-zero values of curvature ($|\nabla^2 z| < 0.008$ m^{-1}) and $|\nabla z|$ values between 0.16 and 0.44 (see gray box in Fig. 6). In contrast, planar regions of the steep and dissected terrain tend to be associated with steep sideslopes ($|\nabla z| > 0.5$) and low-gradient regions (hilltops or narrow valley axes with $|\nabla z| < 0.4$) exhibit highly negative or positive values of $\nabla^2 z$. Wide valley floors were distinguished by near-zero curvature values and gradients uniformly lower than those observed on slide-prone terrain (Fig. 6). For the data sets depicted in Figure 6A and 6B, more than 92% of the deep-seated land-

slide data fall within our topographic envelope, whereas less than 8% and 4% of the valley floor and steep/dissected data points, respectively, plot within the envelope.

We used spatial averaging in applying the topographic signature of deep-seated landslides to the DEM of our study area. First, we identified every grid node within the DEM having gradient and curvature values that fall within our deep-seated morphologic criteria. The resulting binary grid (values of either 0 or 1, with 1 indicating inclusion in the deep-seated topographic envelope) revealed a speckled pattern in some landslide-dominated areas, as localized zones within individual deep-seated landslides did not fall within the topographic envelope. To account for the spatial scale of individual landslides and de-emphasize local deviations from the morphologic criteria, we smoothed the grid of binary data at each node by calculating the proportion of adjacent terrain that met the topographic criteria. Specifically, we generated another grid whose values were

calculated as the fraction of points within a 250 m radius that fell within the deep-seated landslide topographic envelope. Values for the resulting data set, which we term β values, vary continuously from 0 to 1.0, with 0 representing terrain without adjacent landslide-dominated slopes and 1.0 indicating that all of the adjacent terrain exhibits morphology indicative of deep-seated landsliding. For this analysis, we chose a 250 m smoothing radius because it represents the approximate planform dimension of several deep-seated landslides we identified from field surveys and air photo inspection. Larger radii tend to diffuse the signal of individual landslides and smaller radii tend to partition individual landslides into several sections.

Results

Using our automated algorithm, we estimated the distribution of topography indicative of deep-seated slope failure in the Tyee Formation (Fig. 2B). In figures 2B and , high values of

TABLE 1. LANDSLIDE-DAM LAKES IN THE OREGON COAST RANGE.

Name	Latitude (N)	Longitude (W)	Chronology
Ancient Lake Sitkum[†]	43.143°	123.866°	?
Ayers Lake	44.458°	123.785°	Drift Creek slide: Dec. 6, 1975
Bradish Lake	44.605°	123.701°	?
Camp Creek (temporary lake)	43.607°	123.778°	Camp Creek slide: winter, 1956
Esmond Lake	43.871°	123.598°	?
Gould (Elk) Lake	43.535°	123.943°	?
Loon Lake[†]	43.585°	123.837°	>1400 yr B.P.
Lost Lake	43.285°	123.606°	?
Triangle Lake[†]	44.172°	123.571°	>42,000 yr B.P.
Wasson Lake	43.747°	123.793°	?
Yellow Lake	43.799°	123.554°	?

[†]Large lake with upstream alluviated valley greater than 4 km in length (Baldwin, 1958; Thrall et al., 1980; Lane, 1987).
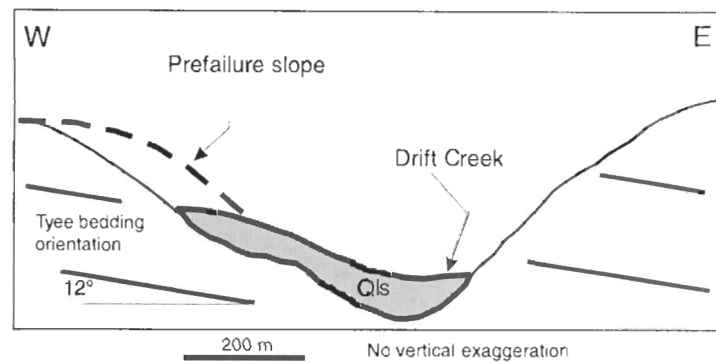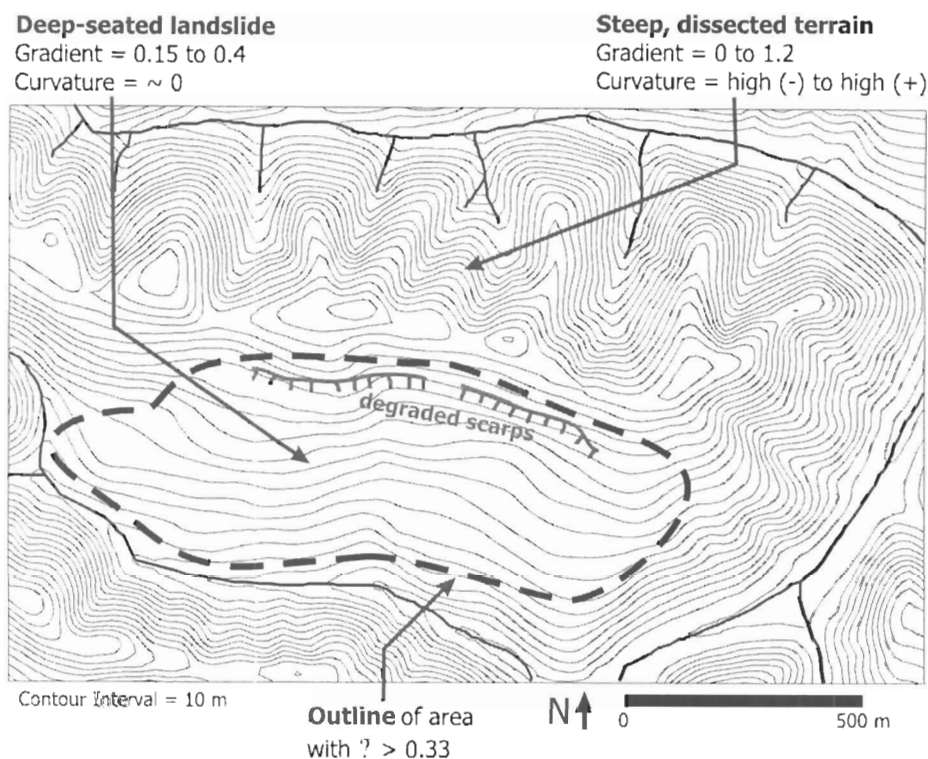

Figure 4. Schematic cross section of Drift Creek landslide (Dec. 6, 1975). Modified after Lane (1987). Qls refers to Quaternary landslide deposit.

10

Deep-seated landslide
Gradient = 0.15 to 0.4
Curvature = ~ 0

Steep, dissected terrain
Gradient = 0 to 1.2
Curvature = high (-) to high (+)

Contour Interval = 10 m

Outline of area
with ? > 0.33

N↑   0 ————— 500 m

Figure 5. Contour map of a ridge in our study area (latitude: 43.855°N, longitude: 123.541°W) that exhibits steep and dissected terrain on its northern side and an ancient deep-seated landslide on the southern flank. Field observations on the landslide revealed degraded scarps near the ridge crest not distinguishable from topographic data. The thick, dashed line illustrates the outer edge of terrain with β >0.33, which delimits boundaries of deep-seated landslide morphology (see text).

β (terrain exhibiting slide-dominated morphology) are represented with warm colors (yellow, orange, and red) and low values with cool colors (green and light blue). To calibrate the particular value of β that corresponds with the margin of landslide-prone slopes, we examined the distribution of β values at numerous locations where we previously identified deep-seated landslides via aerial photos, field observations, and topographic maps. At these sites, β >0.33 served as an accurate criterion for delineating the boundaries of deep-seated landslides. Strictly interpreted, this indicates that for a given grid point with β = 0.33, 33% of the surrounding patch of terrain has values of gradient and curvature that meet the topographic criteria (Fig. 6). The coarse dashed line on Figure 5 illustrates the region within which values of β exceed 0.33. Although some details (such as steep, inner gorges associated with slope failure along channel margins), may not be precisely resolved, the β >0.33 boundary generally corresponds to the zone of landslide-dominated topography (Fig. 5).

β values in the Tyee Formation vary latitudinally (Fig. 2B). In the southern portion of our study area, β values are generally low but locally variable. Moving north, β values increase progressively such that a large fraction of slopes in the northern portion of our study area exhibit β >0.33 (shown as red in Fig. 2B). Several large zones of high β values also occur along the eastern margin of the Tyee Formation. The central and southwestern regions exhibit low β values as slope morphology is dominated by steep and dissected terrain driven by debris flow initiation and runout.

The spatial extent of our study area (~10,000 km²) prevented us from verifying a significant portion of the slopes we identified as failure prone. Using field observations, aerial photos, topographic maps, and maps of landslide-dam lakes, we tested the algorithm at over 40 sites and concluded that it consistently separated deep-seated landslides from steep/dissected terrain and valley floors. Locally, the algorithm misidentified fluvial meander slip-off surfaces (i.e., the inner banks of large bedrock

meanders) as slide-dominated because they tend to exhibit smooth, low-gradient surfaces (Fig. 7). These features are isolated to isolated zones along major rivers and thus constitute a negligible fraction of the landslide-prone (high β) terrain shown in Figure 2B.

LITHOLOGIC CONTROLS ON LANDSLIDING AND TOPOGRAPHIC RELIEF

Method

To explore how lithologic variations within the Tyee Formation affect the development of landslide-prone terrain, we quantified how β values vary in accordance with latitudinal facies changes. As discussed above, sand-rich deltaic and proximal ramp deposits found in the southern half of the Tyee Formation grade northward into silt-rich distal and ramp fringe deposits. We quantified north-south topographic variations by partitioning our grid of β values into a series of horizontal swaths, each measuring 12.5 km in the north-south direction and spanning the study area in the east-west direction. Within each swath, we calculated the fraction of terrain (hereafter referred to as F) exhibiting the topographic signature of deep-seated landsliding (i.e., with β >0.33). To investigate the effect of deep-seated landslides on topographic development, we calculated the distribution of local relief at two different spatial scales. For each grid node in our study area, we calculated local relief as the difference between the highest and lowest elevation values within a circular window. We performed separate analyses using a 250 m window to represent relief at the scale of individual ridges and valleys and a 2.5 km window to represent the regional distribution of relief encompassing several nearby ridge/valley sequences (Roering et al., 2001).

Results

Our analysis reveals systematic latitudinal variation in deep-seated landsliding, as β values tend to be relatively low in the south and increase to the north (Fig. 8). This pattern may reflect facies variability within the Tyee Formation (Chan and Dott, 1983; Heller and Dickinson, 1985). In the southern region, landslides comprise 5%–10% of the landscape, whereas for latitudes greater than 44°, the proportion of slide-prone terrain consistently exceeds 15%–20% (Fig. 8A). This relatively discrete transition corresponds with a significant change in the sandstone:siltstone ratio (from 9:1–6:4) and a shift from proximal to distal ramp facies.
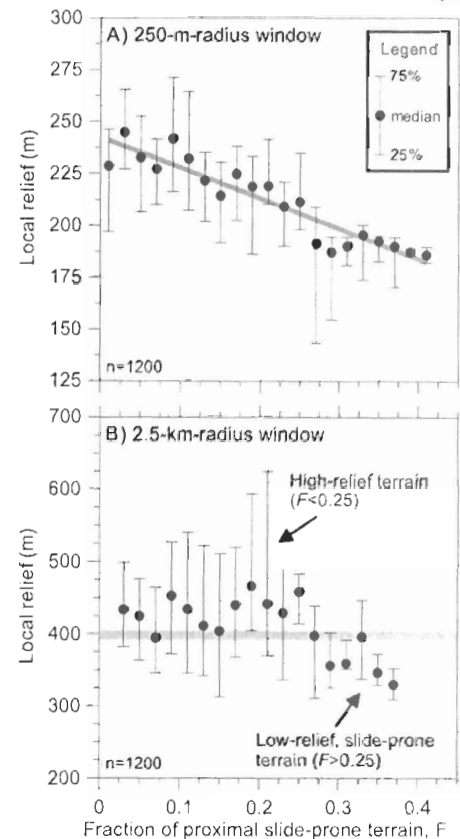
Sedimentary facies: Tyee Formation
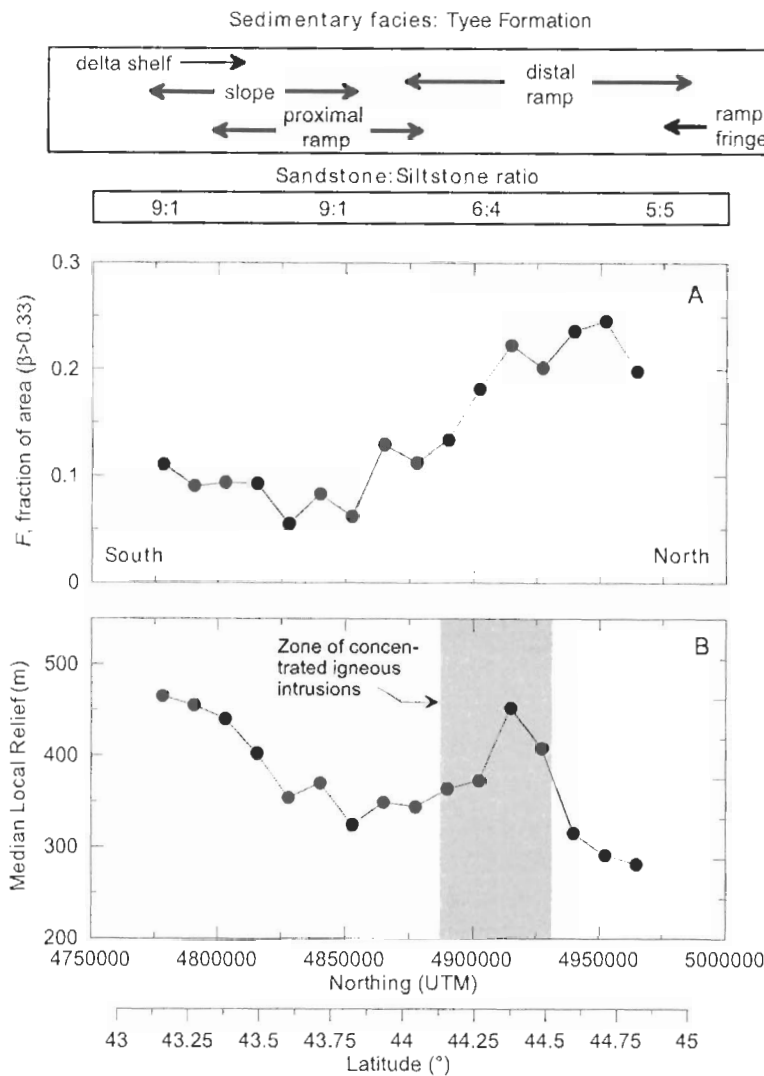
Figure 8. Latitudinal variation in (A) fraction of terrain with β >0.33, and (B) median local relief using a 2.5-km-radius window. Annotations at the top illustrate latitudinal variation in sedimentary facies and the sandstone:siltstone ratio (Chan and Dott, 1983; Heller and Dickinson, 1985). For each plot, data were calculated from sixteen 12.5 km (measured north-south) nonoverlapping swaths. The prevalence of terrain influenced by deep-seated slope instability increases northward, coincident with a decrease in the sandstone:shale ratio and median local relief. The gradual, northward decline in relief is locally perturbed around a zone of concentrated igneous intrusions (see gray box in B). These resistant units generate anomalously high values of relief as they modulate valley incision in adjacent slopes of the Tyee Formation. See Figure 2A for the location of intrusions. UTM refers to Universal Transverse Mercator coordinate system in meters.

Figure 9. Variation of local relief with the proportion of terrain prone to deep-seated landsliding. At 1200 randomly chosen points with our study area, we used 250-m- and 2.5-km-radius windows to calculate values of local relief and the fraction of adjacent terrain with β >0.33, F (see text for description). (A) Median hillslope-scale relief (250 m window) declines linearly with F. Summary statistics for the regression line fit to median values: $y = -146.5x + 242.5$, $r^2 = 0.87$. (B) Regional-scale median relief (2.5 km window) is ~440 m where $F <0.25$ and declines to ~340 m where $F >0.25$. The thick gray line roughly separates low-relief, slide-prone terrain from high-relief terrain with a smaller density of slope failures. Filled circles and error bars represent the median and upper/lower quartiles for distributions with bin size of 0.02.

landscape exhibits the signature of deep-seated landsliding where dip angles approach 15°. For a given dip angle, variability in the fraction of slide-altered terrain is significant, reflecting additional factors that influence the propensity for deep-seated landsliding. The ubiquity of thick siltstone beds in the northern region may modulate both landslide style and thresholds of slope instability.
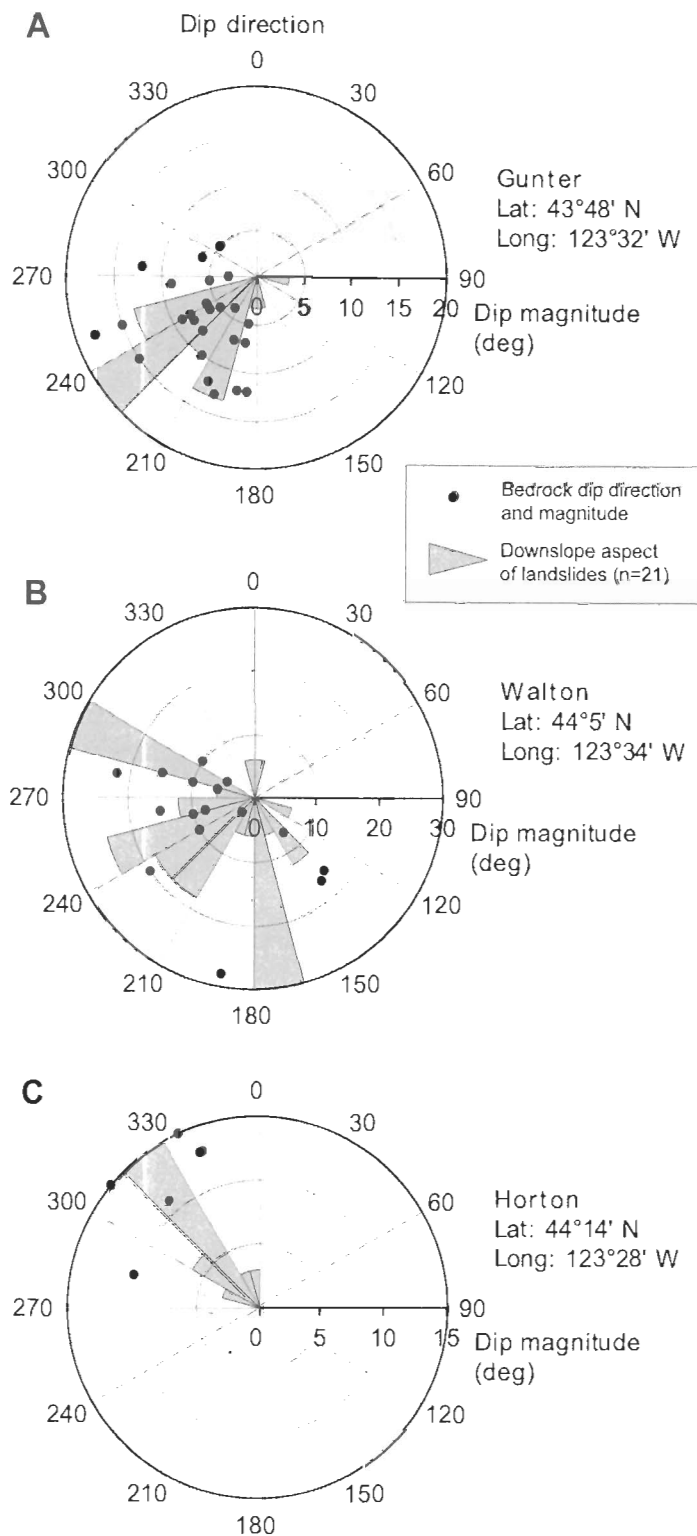
IMPLICATIONS FOR LANDSCAPE DEVELOPMENT

Continued rock exhumation in the OCR will result in a southward shift of sedimentary facies (Fig. 12). Due to the progradational nature of the Tyee Formation (Heller and Dickinson, 1985), distal and ramp fringe deposits with low sandstone:siltstone ratios will progressively

crop out in the central region of our study area as erosion of the OCR proceeds. Owing to the linkage between bedrock lithology, structure, and slope instability, large slope failures will play an increasingly prominent role in shaping the central and eventually southern OCR. The time scale for this process transition can be coarsely estimated using erosion rates (~0.1 mm yr^{-1}) and thickness estimates (2–3 km) of the Tyee Formation. These

Figure 10. Rose and polar plots illustrating the correspondence between the aspect of failure-prone slopes (gray pie slices) and the dip and direction of bedrock (filled circles) for three regions within our study area. Data collected within the (A) Gunter, (B) Walton, and (C) Horton, United States Geological Survey (USGS) 7.5" 1:24k topographic quadrangles. Distance from the origin represents the magnitude of bedrock dip (filled circles) and the relative frequency of failure-prone slopes with a given aspect (gray pie slices). Hillslope aspect data were binned in 15° intervals.

data indicate that it would take 20–30 m.y. to unroof the entire Tyee Formation. Considering the subsurface architecture of Tyee Formation facies (Heller and Dickinson, 1985), one might expect the current surficial facies distribution to shift 20–40 km southward over 2–3 million years. Given that uplift in the OCR has been active since the late Miocene (McNeill et al., 2000), the north-to-south replacement of steep/dissected terrain with deep-seated landslides is likely an ongoing process. This conceptual model suggests that landslide-dominated, low-relief terrain will cannibalize steep and dissected topography in the central OCR. As a result, the dominant role of debris flows in sculpting drainage basins will be transferred to episodic, large-magnitude mass movements that frequently dam valleys and punctuate sediment delivery (Fig. 12). Complications to this simplified model include localized aphanitic dikes that limit the incision of adjacent terrain and tend to favor the maintenance of long, high-relief slopes.
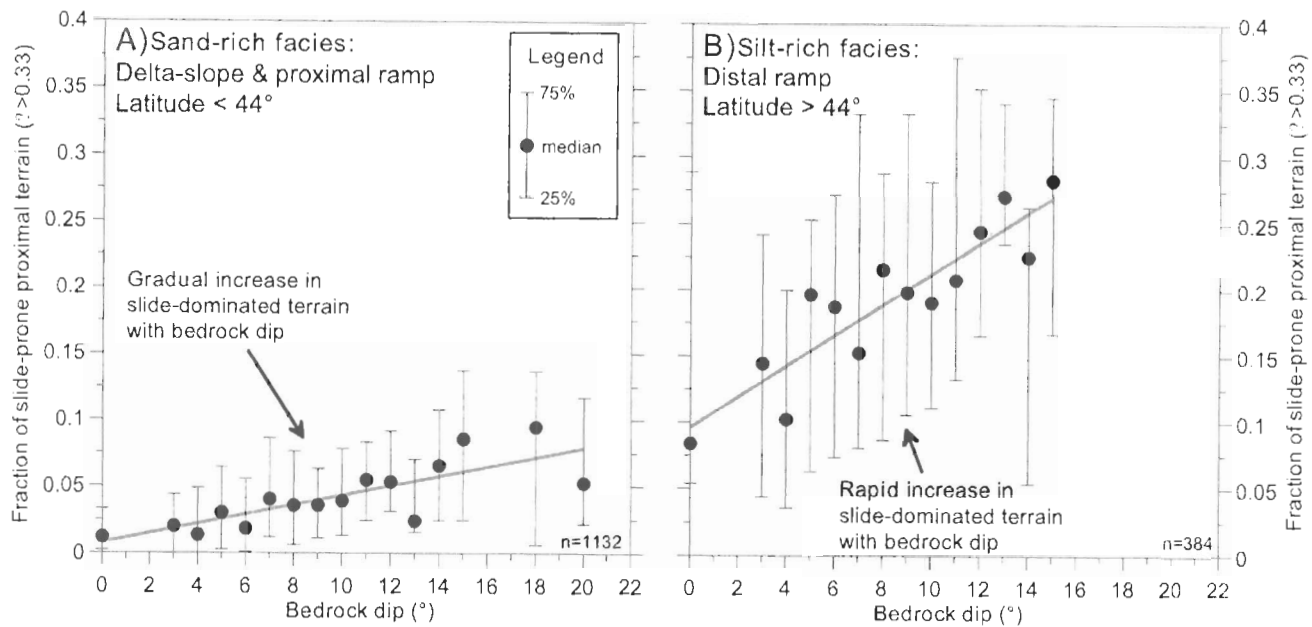
DISCUSSION

Our results indicate that deep-seated landsliding is pervasive in the OCR and will continue to play a prominent role in shaping the landscape according to systematic variations in bedrock structure and lithology. In a recent study, Montgomery (2001) focused on shallow landslide susceptibility and analyzed slope distributions across a broader expanse of the OCR than analyzed here, suggesting that systematic variations in relief and hillslope gradient primarily reflect variation in tectonic forcing and rock type. In contrast, our analysis emphasizes the role of large, bedrock landslides in regulating topographic development of the OCR underlain by the Tyee Formation. Local relief decreases with the fraction of area altered by deep-seated landsliding and does not appear to reflect variations in rock uplift rate (Kelsey et al., 1996).

The topographic algorithm we employed to derive these insights is not necessarily intended for use in site-specific analyses of landslide potential but instead enables us to identify slopes whose morphology is indicative of deep-seated landsliding. Our methodology performed well in areas where we compared model predictions with field observations; however, we observed several instances where the algorithm misidentified fluvial meander slip-off surfaces as failure-prone slopes. Although this misrepresentation does not affect our conclusions about the relative importance of deep-seated landsliding because such meanders are localized and sparse in the OCR, additional morphologic criteria that account for proximity and geometry of nearby valleys are needed.

Figure 11. Variation in the fraction of slide-prone terrain with bedrock dip angle for (A) sand-rich facies south of 44° latitude, and (B) silt-rich facies north of 44° latitude. For each strike and dip observation (n = 1516), we calculated the fraction of surrounding terrain (within 2.5 km) with $\beta > 0.33$. Each data point represents the median value for 1° bins of bedrock dip angle. Upper and lower error bars represent the 75th and 25th percentile values, respectively. The extent of failure-prone terrain increases linearly with dip in both regions, although the silt-rich areas exhibit a higher proportion of landslide-prone terrain for a given bedrock dip angle. Summary statistics for linear regressions fit to the median values are: $y = 0.0035x + 0.0077$, $r^2 = 0.65$ for the sand-rich region and $y = 0.0116x + 0.096$, $r^2 = 0.81$ for the silt-rich region. We did not calculate median values for bins with fewer than 10 data points.

Calibration of our algorithm depended on the resolution of topographic data. In particular, the grid spacing of DEMs determined the nature of the morphologic signature used to identify landforms. Interestingly, our observation that large landslides are smooth and relatively planar when compared to adjacent stable terrain may be reversed when meter-scale morphologic data are employed. In contrast to our analysis using ~26.5 m data, a recent study that used ~1 m data derived from airborne laser swath mapping (ALSM) indicates that slide-prone terrain is highly roughened and irregular compared to adjacent, unfailed slopes, and that it exhibits varying degrees of roughness depending on the time since instability (McKean and Roering, 2004). Furthermore, the scale of our topographic data and the width of our smoothing window limited the spatial extent of landslide-dominated terrain that could be identified. Although our map of β values accurately located large, ancient slide masses, it less effectively distinguished small segments of hillslopes that experienced deep-seated slide activity. During our field visits, we noted numerous headscarps and benchlike landforms at the scale of ~100 × 100 m that did not consistently generate values of $\beta > 0.33$. Many of these smaller landslides

exhibited somewhat elevated β (0.1 0.3) values and thus were classed in the transitional category (yellow color in Fig. 2B). In contrast to our simple, bivariate method of distinguishing deep-seated landslides, more elegant statistical methods that incorporate principal component analysis have been effectively applied toward a similar end (e.g., Howard, 1995).
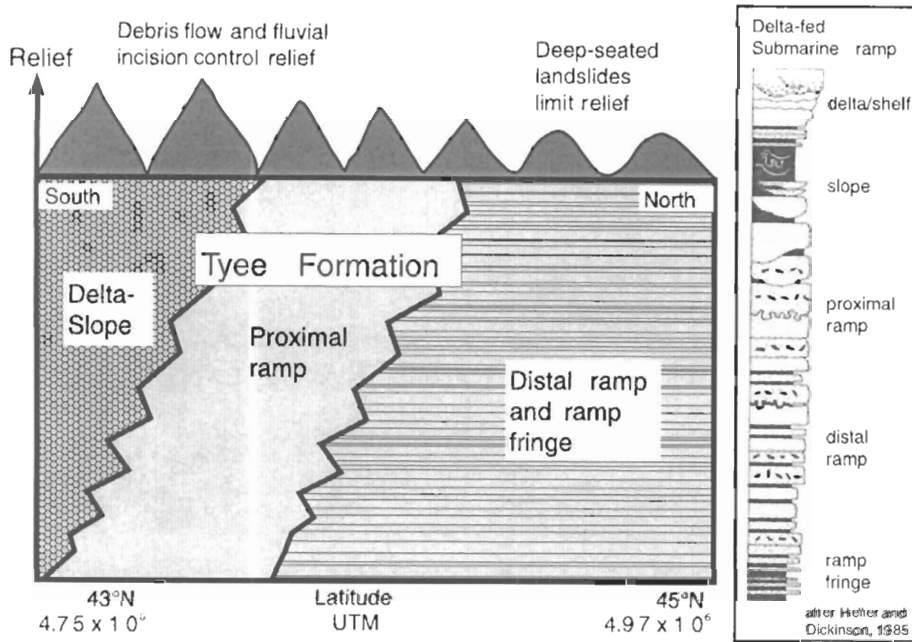
The prevalence of landslide-dam lakes in the OCR offers an additional opportunity to test our algorithm. The slopes adjacent to each of the lakes (Table 1) exhibited patches having the morphologic signature of deep-seated landsliding ($\beta > 0.33$). In particular, the landslide deposit responsible for creating Triangle Lake and the upstream alluviated valley, which exceed 10 km² in area, has $\beta > 0.33$, and the size of the feature is typical for failure-prone slopes in the OCR (~1 km²). From estimates of typical landslide size and our calculations of landslide density, at least 2000 deep-seated landslides persist in the OCR.

Thick, highly weathered soils, relatively smooth headscarps, and extensive alluvial fills associated with landslides in the OCR suggest that these large slope failures have persisted in the landscape for long periods of time (>10 k.y.). Once initiated, deep-seated failures may episodically occur at a particular location due

to the inclination of low-shear-strength siltstone beds and preferential groundwater flow along sedimentary interfaces. Currently, it is unclear whether slopes prone to deep-seated activity can be recolonized by the processes that shape steep and dissected terrain (i.e., fluvial and debris flow incision). We observed sparse evidence of large, contiguous failure-prone slopes experiencing renewed dissection. This may indicate that deep-seated landslides remain sufficiently active to subvert valley dissection and steepening. The conditions for valley-forming processes (such as shallow landsliding and erosion associated with overland flow and seepage) on the low-gradient and low-drainage area slopes of large landslides are unfavorable according to slope-drainage area channelization thresholds (Montgomery and Dietrich, 1988). Most generally, terrain in the OCR appears to be largely bimodal, as it is characterized by steep, debris flow–prone ridge and valley sequences and by gentle, benchlike deep-seated landslides.

The timing and triggering mechanisms of large slides in the Tyee Formation are uncertain. The few examples of historically active deep-seated slides have occurred on slopes whose morphology suggests previous alteration by deep-seated slope instability (Thrall et

CONTROLS ON DEEP-SEATED LANDSLIDING: OREGON COAST RANGE

Figure 12. Schematic illustration of the topographic manifestation of sedimentary facies of the Tyee Formation. Silt-rich distal and ramp fringe deposits in the north tend to generate large, deep-seated landslides and low-relief terrain. Sand-rich deltaic facies in the south are predominantly characterized by high relief terrain with relatively low rates of slope alteration by large, bedrock landslides. Continued exhumation of the Tyee Formation will result in a southward shift of slide-prone, low-relief terrain underlain by silt-rich distal facies. UTM refers to Universal Transverse Mercator coordinate system in meters.

al., 1980). In some cases, minor movement of deep-seated landslides appears to have initiated due to loading effects of road waste deposition (Seward and Blackwood, 1998). Historical rainfall events have occasionally been sufficient to reactivate older slides, but the relative importance of valley incision, hydrologic events, or seismic activity in initiating new failures remains to be explored. The location of the OCR above an active subduction zone suggests that infrequent, large-magnitude earthquakes (Atwater et al., 1991; Nelson et al., 1995) may have contributed to landslide initiation, but the lack of historical observations makes this hypothesis difficult to test. Coseismic landslides of similar scale have been documented for recent seismic events (King et al., 1987; Martinez et al., 1995; Schuster et al., 1998; Guzzetti et al., 2002; Khazai et al., 2004). Establishment of a high-resolution landslide chronology record via lake cores or internal slump ponds may reveal the synchronicity of failure events. The two available dates for the formation of landslide-dam lakes in our study area (1.4 ka for Loon Lake and >40 ka for Triangle Lake) are disparate and the degree to which deep-seated activity has persisted through the Late Quaternary evolution of the OCR remains to be shown.

The correspondence between bedrock structure, lithology, and hillslope aspect provides local control on deep-seated landsliding in the Tyee Formation and other regions (e.g., Schmidt and Montgomery, 1996; Jackson, 2002) and may drive variability in the frequency of deep-seated landslide terrain estimated around the strike and dip measurements (Fig. 11). In the northern section of our study area, distributions of β values indicate that aspects of failure-prone slopes are locally less uniform than observed elsewhere. The high density of slide-dominated terrain in the northern section of our study area suggests that the mechanical requirement that dip slopes correspond with hillslope aspect may be relaxed. Here, the predominance of thick, low-strength siltstone beds may facilitate slope failures over a broader range of slope geometries. The style of slope failure also appears to vary across our study area as large translational slope failures dominate in the southern region, and rotational slips are more common in the northern region.

Our conceptual model that forecasts a north-to-south, landslide-driven unzippering of relief in the OCR is derived through a synthesis of topographic, structural, and lithologic data. Additional factors that may affect our relief

calculations include variable rates of baselevel lowering and the positioning of major and minor river systems. Terrain at the southern tip of our study area exhibits high values of relief that may be affected by differential uplift rates to the south and associated drainage basin adjustment.

In many active tectonic areas underlain by fine-grained sedimentary bedrock (e.g., Eel River, northern California; upper Waipaoa River, New Zealand; and the Eastern Coast Range, Taiwan), patterns of sediment production are dominated by large landslides and local relief is low (~300–400 m) despite rapid rates of rock uplift (~1–5 mm yr^{-1}). In such areas, the frequency and magnitude of slope failure may be sufficient to prevent the development of relief typically associated with high uplift regions. Although rates of tectonic forcing in the OCR are low in comparison, large landslides likely temper the coupling between tectonic forcing and local relief because they affect the entire hillslope and impose low gradients over broad areas.

CONCLUSION

In contrast to the steep and dissected, debris flow prone terrain often cited as characteristic of the Oregon Coast Range, terrain prone to deep-seated landsliding is pervasive and exhibits low-gradient, benchlike morphologies. We defined the topographic signature of deep-seated landslides and developed an automated algorithm to map the extent of terrain altered by slope failure. The particular algorithm we employed was developed specifically for slopes in the OCR; however, the general approach described here may be applicable for mapping and identifying large landslides in other landscapes. The fraction of terrain affected by deep-seated landsliding varies from 5% 25% as a function of bedrock structure and lithologic variations. The frequency and thickness of low-shear-strength siltstone beds in the sand-rich deltaic-turbidite deposits of the Tyee Formation increase to the north, coincident with a systematic increase in the fraction of terrain dominated by deep-seated landsliding.

The fraction of slide-prone terrain increases proportionally with bedrock dip angle and in the northern region of our study area, where nearly 30% of the landscapes exhibits the signature of deep-seated landsliding. Local relief declines correspondingly, implying that deep-seated landsliding imparts a first-order control on landscape development. Our analyses suggest that continued exhumation in the OCR will result in a southward shift of distal silt-rich facies, enabling us to generate quantitative predictions for the evolution of the OCR. The progressive emergence of the slide-prone units should drive a

Tyee Domain in the Luckiamute Basin:

- Steeper, rugged hillslopes
- More finely dissected by low-order channels
- Tendency to spawn debris flow
- Lower stream-power index compared to Yamhill Domain
- Higher average valley widths, increased sediment accommodation space

Working Hypotheses for Tyee Domain:

- Hillslope transport rates are greater than the ability of the channel system to export sediment

- Steep hillslopes and increased valley widths result in comparative decrease of net sediment-transport efficiency
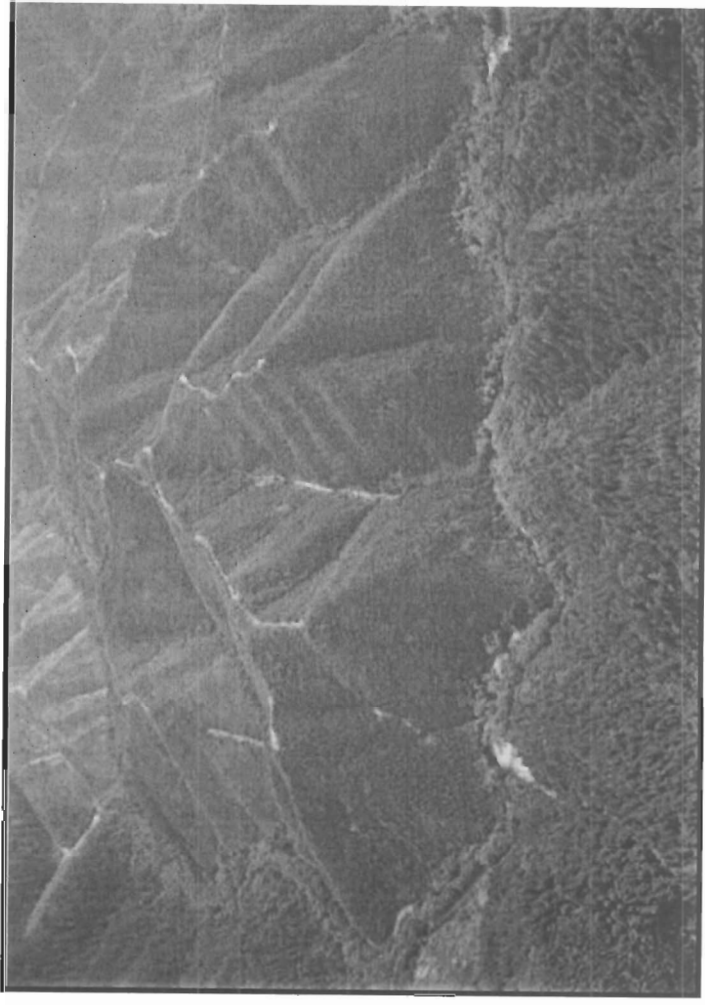
CHARACTERISTICS OF DEBRIS FLOWS

Debris flows, shown schematically in Figure 5 and by example in Figure 6, consist of water-charged soil, rock, colluvium, and organic material traveling rapidly down steep topography (Johnson, 1984). Debris flows are often triggered by small landslides (Figure 7) that then mobilize and grow to be large flows, entering and scouring stream channels downslope (Figure 8). When momentum is eventually lost, the scoured debris is often deposited as a tangled mass of boulders and woody debris in a matrix of finer sediments and organic material (Figure 9).
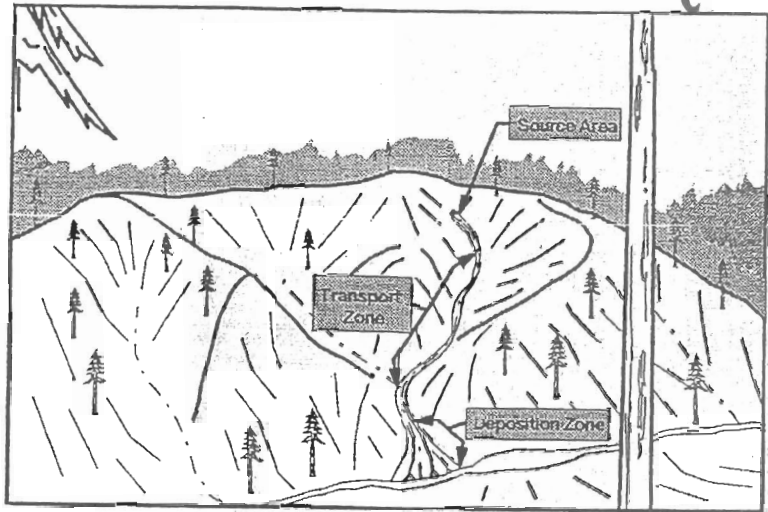
Figure 5. Diagram of a debris flow showing zones of initiation (source areas), transport, and deposition. (From Pyles and others, 1998)
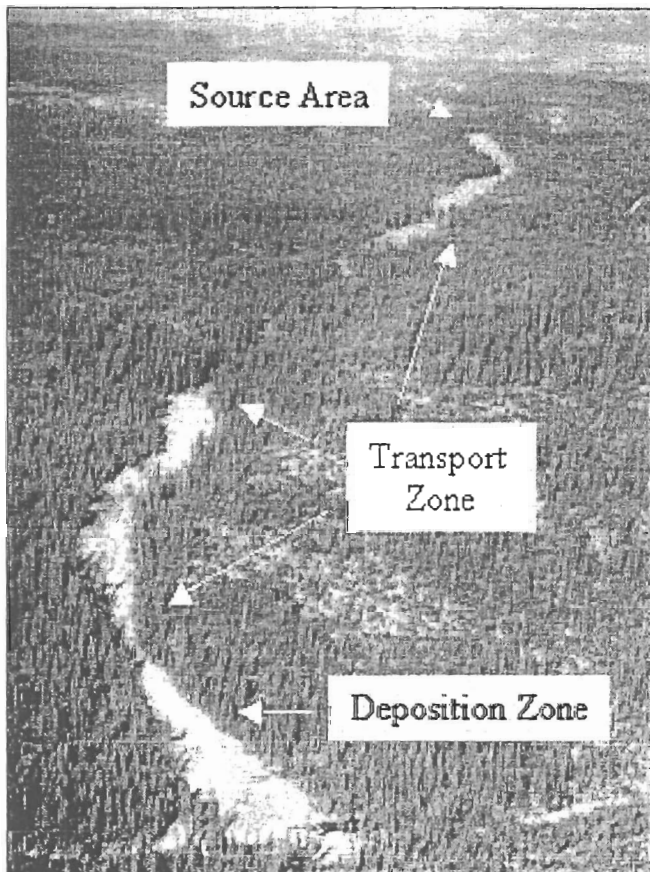
Figure 6. Photo of a debris flow showing zones of initiation, transport, and deposition. (Photo courtesy of U.S. Geological Survey)

Although debris flows can be extremely variable and chaotic, they have some common characteristics. These characteristics form the basis of much of our scientific understanding and provide the keys to identifying and modeling potentially hazardous locations. Before describing the development of the hazard map, therefore, useful background on factors that affect debris flow potential is provided.

For descriptive purposes, it is helpful to segment debris flow paths into areas of initiation, transport, and deposition as shown generally in Figures 5 and 6. Some of the common debris flow causes (termed trigger mechanisms) are outlined below, followed by some of the significant factors affecting debris flow initiation, transport, and deposition. This section provides only a brief overview of the subject.
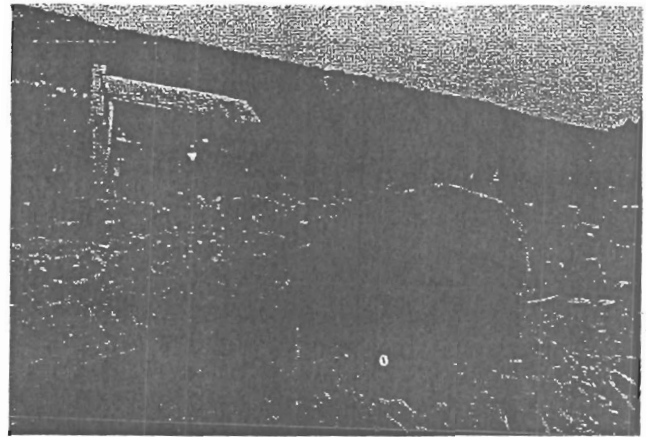
Trigger Mechanisms

Debris flows can be initiated in marginally stable slopes by a number of natural and unnatural disturbances. Because most steep slopes are near their point

17
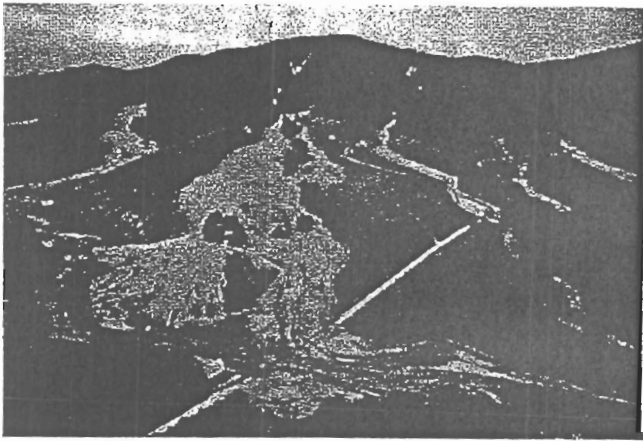
(A)

(B)

FIGURE 4.39

Debris flow and avalanches in Nelson County, Va., during 1969. (A) Flows deposited debris on small fans at the base of first-order hillslope channels (near Lovingston). (B) Catastrophic erosion and impact forces from these flows removed some structures and devastated others (view from Davis Creek).

Foliation plane

Joint surface

Foliation

Hollow
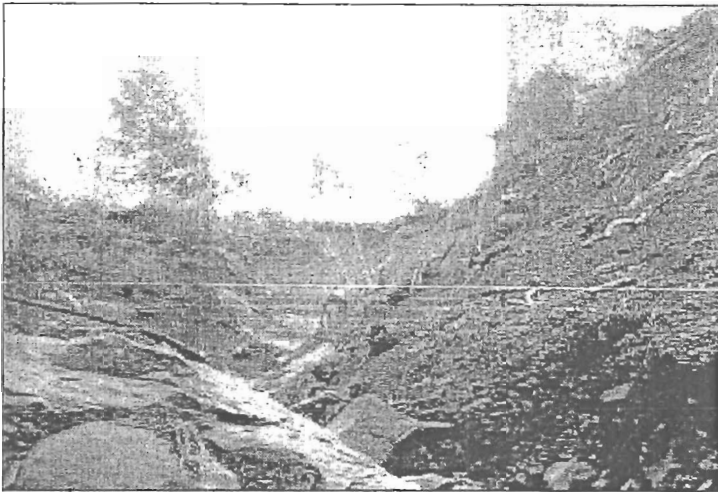
Groundwater flow

Crystalline bedrock
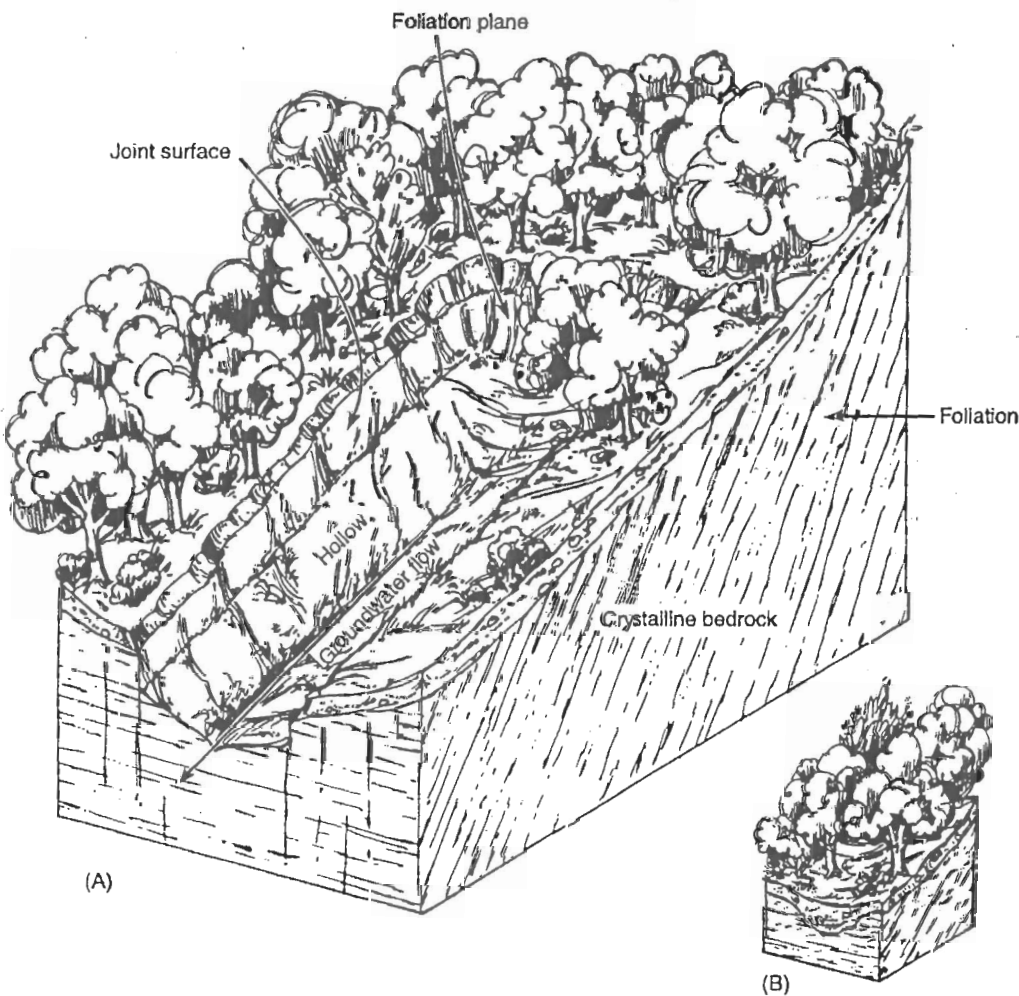
(A)

(B)

FIGURE 4.40

Schematic model of a colluvium-filled hollow. (A) Hollow excavated to bedrock by a recent debris avalanche/debris flow. (B) Hollow has been refilled with calluvium and slope wash after a few hundred years. The site is now primed for another debris flow event once again.

of equilibrium, failures can be the result of seemingly minor modifications. In a fundamental sense, modifications that lead to failures can be simply grouped into factors that (a) increase the gravity-driven forces acting downslope and (b) reduce the resisting forces acting to keep the slope in place (Figure 10). Multiple factors may be involved in triggering any given debris flow.

Natural events that can induce failures include high-rainfall storms, rapid snow melt, earthquake shaking, breach of landslide or other natural dams, and volcanic eruptions (Wieczorek, 1996). By far the greatest number of debris flows that have occurred in Oregon (at least in historical times) have been associated with severe rainfall and rain-on-snow storm events.

Severe Rain Storms

High-precipitation storms can trigger slope failures through a number of mechanisms. Water infiltration into zones of weakness can trigger failures by (1) reducing the frictional resistance to sliding, (2) increasing pore pressures within a slope mass, and (3) adding weight (through saturation of the soil mass) (Turner and Schuster, 1996). Typically, all three of these mechanisms combine during long-duration, heavy-precipitation storm events to trigger widespread slope stability problems. During three 1996/97 storm events, for example, thousands of landslides (including many debris flows) were triggered throughout western Oregon (Figure 11).

Given the importance of rainfall events for slope failures, it is not surprising that a number of studies have

↑ Figure 7. Small intiating landslide.

➡ Figure 8. Scoured transport zone.

⬇ Figure 9. Tangled debris in deposition zone.

30 m/s are computed (Wigmosta et al. 1981; Janda et al. 1981). This unbelievable average velocity is probably a result of (a) super-acceleration from the lateral blast of the volcanic eruption, or (b) result of poor site selection, or (c) wave splatter setting unrealistically high mud marks. The fundamental validity of velocity values calculated from superelevation, and assumptions therein, remain unverified for use with mud and debris flows (Ikeya and Uehara 1982). Since this method is promising because of its wide applicability, more research is needed on the influences of fluid strength on superelevation.

Earlier it was noted that mudlines on surviving trees in the path of debris and mud flows show runup of the fluid on upstream sides. This runup reflects the point surface velocity of the moving fluid, and for debris flows can probably be assumed nearly equal to the mean velocity at that point. Runup from mudlines on trees, hills, or canyon walls might be used to obtain any number of point mean velocities of flows by substituting the amount of runup into the velocity head equation ($\Delta h = \alpha v^2 / 2 g$). Strictly speaking, hydrostatic pressure relationships are not valid for flows with strength. However, no data exist to my knowledge to verify just how well or how poorly runup on trees or other obstructions compares with measured velocities for mud and debris flows. Studies have been made on clear-water streamflow (Wilm and Storey 1944). This method needs further investigation.
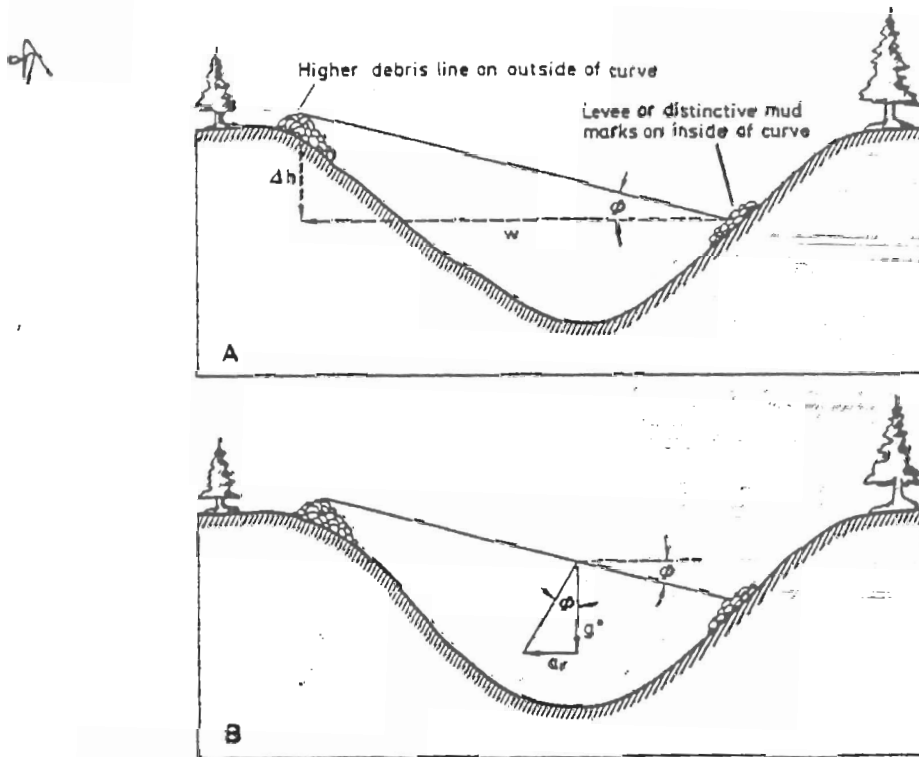

Fig. 14. Technique for estimating average velocity of debris flows from superelevation in curves. (From Johnson 1979)

(Left margin, partial text from facing page)

y of Debris Flows

ed sediment ac-
ebris flows con-
crease clear-wa-
s for clear-water
r flows with 50%
8). Bulking fac-

a series of curves
age area for dif-
draulics Division
ris basins. Bulk-
3). A maximum
within maximum
ing factors in the
topography, ge-
by weight in de-
ographic areas.

utside of channel
ators, and can be
uy 1971; and Ap-
w around a bend.
law of motion to
ave equal velocity
pproximated as a

dius of curvature.

fevation difference
. Solving for mean
about 15 degrees.

the tilt of the flow
sured. This method
this probably does
calculating velocity
pplied to mudflow
elocities as great as
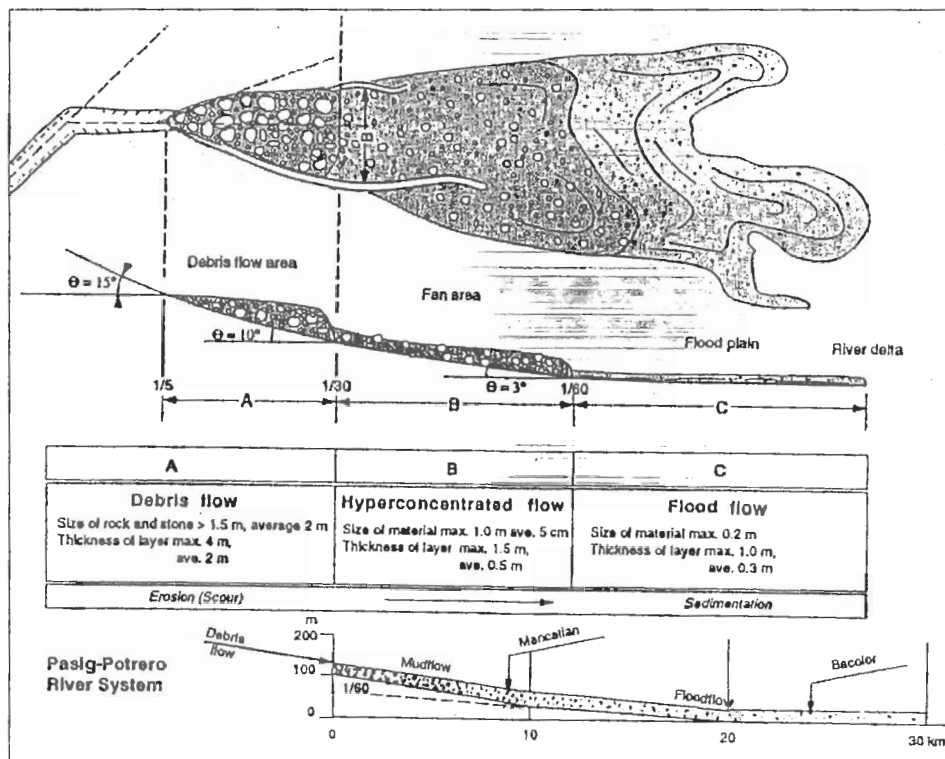
Figure 15. Unchannelized debris flow deposit.

Figure 16. Schematic of transition from debris flow to hyperconcentrated flow to flooding. (From United Nations, 1996)
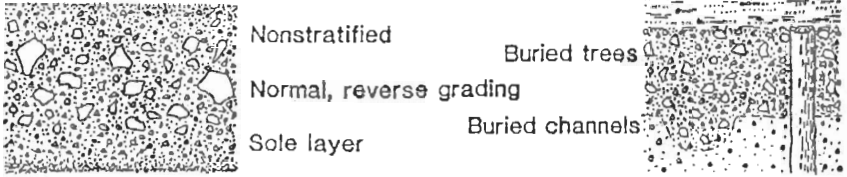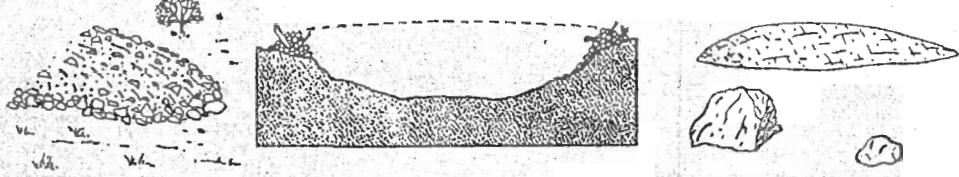
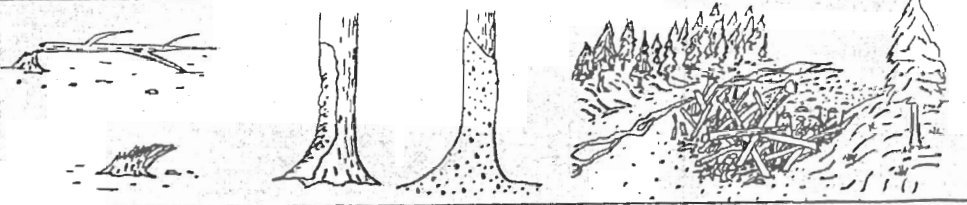| STRATIGRAPHIC	Nonstratified Normal, reverse grading Sole layer			Buried trees Buried channels
SEDIMENTOLOGIC	Closed, interlocking structure Matrix between clasts Vesicles	Coarse grain size < 10 – 15% silt & clay	Extremely poor sorting 3.0 – 6.5Φ (2.0 – 4.0Φ)	Fine skewed distribution
MORPHOLOGIC				
BOTANIC				

Figure 18. Geomorphic features that can aid in the **identification of historic** debris flows. (Diagram courtesy of Tom Pierson)

Both the Oregon Departments of Geology and Mineral Industries (DOGAMI) and ODF performed these targeted field investigations. Geographically distributed (and geologically diverse) areas were evaluated as shown in Figure 19. In these areas, reconnaissance-level field investigations were conducted. Where geologic evidence clearly defined the extent of historic debris flow deposits, boundaries were mapped. More commonly, the geologic evidence was discontinuous or otherwise inconclusive. In these cases, field investigations focused on a general rating of terrain for high versus low relative debris flow hazard.

Improved GIS Modeling

During and following the initial field mapping, a variety of GIS models that could aid in the hazard mapping effort were evaluated.

Our focus was on identifying a suitable modeling framework to delineate the range of debris flow hazards observed in the field, including initiation, transport, and deposition areas. While numerous models have been developed for evaluating initiation potential, fewer have focused on the transport and deposition hazards — areas that are critical for impact and public safety.

In a general review of modeling approaches and available models, a modeling framework developed by the Earth Systems Institute (ESI) was selected as the starting point. The ESI program uses topographic input data (DEMs) and a suite of rules to model initiation, transport, and deposition zones. In this study, the general three-part framework implemented was as follows:

For initiation, steep slopes are used as the

Legend

Third Order and Higher
Second Order
First Order
Hollows

a

b
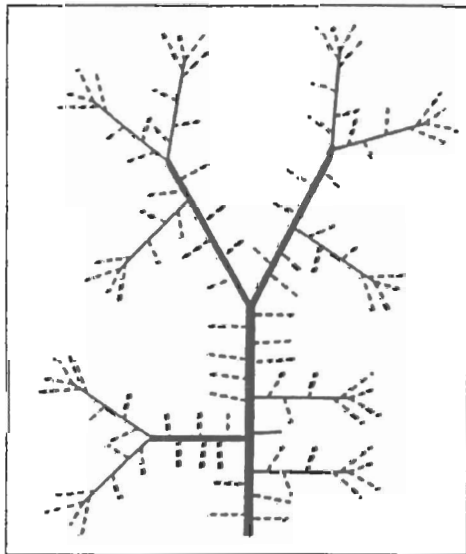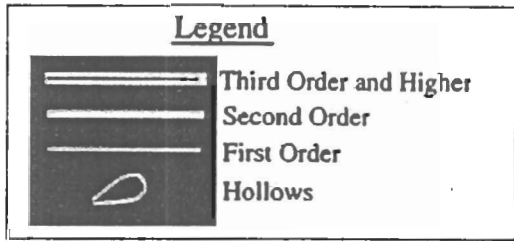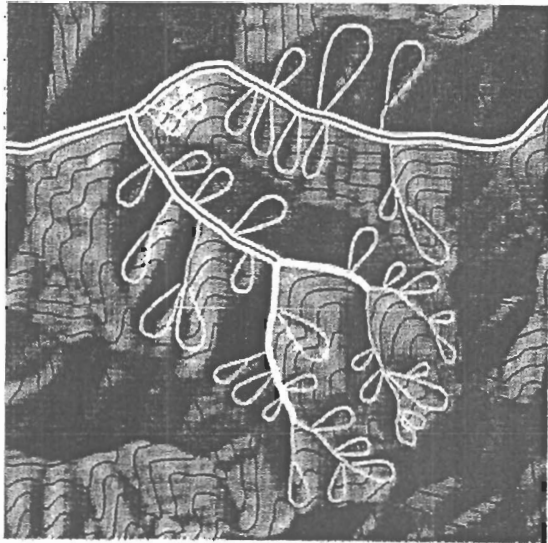
Figure 2. (a) Topographic contours and shaded relief showing the bedrock hollow-channel network structure up to third-order in the central Oregon Coast Range (OCR). Landslides in hollows trigger debris flows in first- and second-order channels, which deliver sediment to third- and higher-order valley floors. In addition, some bedrock hollows are located adjacent to third- and higher-order channels. First- and second-order channels comprise about 90% of all channel length in the region. (b) Schematic diagram of the structure of the hollow-channel network in an average 1-km^2 area containing a third-order stream (thickest line), three second-order channels (medium lines), 10 first-order channels, (finest lines) and 100 hollows (dashed lines).

years B.P.) of colluvial wedges in the upper parts of nine bedrock hollows to indicate a change in the mid-Holocene climate of the OCR that favored landsliding. *Personius et al.* [1993] established an age of 9000–11,000 years B.P. for an alluvial terrace throughout the central OCR, implying a region-wide evacuation of colluvium from bedrock hollows, presumably brought about by climate change during the Pleistocene-Holocene transition. *Benda and Dunne* [1987] interpreted four basal radiocarbon dates (1600–9500 years B.P.) collected at recent landslide scars in the lower parts of hollows to represent the time necessary to refill landslide scars with colluvium to the point of failure in an unchanging climate. This proposal was not meant to deny the possible role of climatic change but only to admit ignorance in the face of sparse data. *Dunne* [1991] suggested a reconciliation of the differing interpretations of colluvium ages from the upper and lower parts of hollows with a simulation model which suggested that under a steady climate colluvium becomes unstable more frequently in the lower portion of a hollow than in the upper part. Evacuation of the latter may require changes of climate and fire regime of the magnitude proposed by *Reneau and Dietrich* [1990] and *Personius et al.* [1993].

3. Climate and Vegetation History

The application of our simulation model to the central OCR is based on the hypothesis that climate of the region has not changed for at least 3000 years. This hypothesis is based on studies of plant pollen assemblages in western Washington State by *Heusser* [1974, 1977], *Barnosky* [1981], *Leopold et al.* [1982], and *Cwynar* [1987], and in western Oregon by *Worona and Whitlock* [1995], indicating that a climate similar to the present one has existed in the OCR for the past 3000–6000 years. *Long's* [1995] study of pollen and charcoal profiles in a small lake in the OCR suggests no change in fire frequency over at least the past 2000 years, even through the Little Ice Age. The principal reason for climatic stability throughout the mid- to late Holocene in the Pacific Northwest is the moderating influence of the Pacific Ocean and the semipermanence of the north Pacific subtropical high and the Aleutian low that largely control the Pacific coast climate [*Johnson*, 1976].

During the mid- to late Holocene, the humid mountain landscape of the central OCR has been forested predominantly by Douglas fir (*Pseudotsuga menziesii*) and western hemlock (*Tsuga heterophylla*) [*Franklin and Dryness*, 1973] under a climate of rainy winters ($\approx$2200 mm yr^{-1}) and dry summers. Wildfires infrequently kill large areas of trees (Figure 3) [*Teensma et al.*, 1991; *Agee*, 1993] and control the distribution of forest ages, which range up to more than 200 years [*Andrews and Cowlin*, 1934].

4. Stochastic Model of Sediment Supply to a Channel Network

This paper describes a stochastic model for interpreting the roles of temporal and spatial factors that control the sediment influx to channel networks through landsliding and debris flow at the scale of a 215-km^2 watershed over thousands of years. We begin by positing a landscape of bedrock hollows linked to a network of channels (Figure 2); the axes of the hollows have probability distributions of gradients and colluvium depths, which are independent of one another as the model begins. Each year, colluvium accumulates in each hollow at rates

C
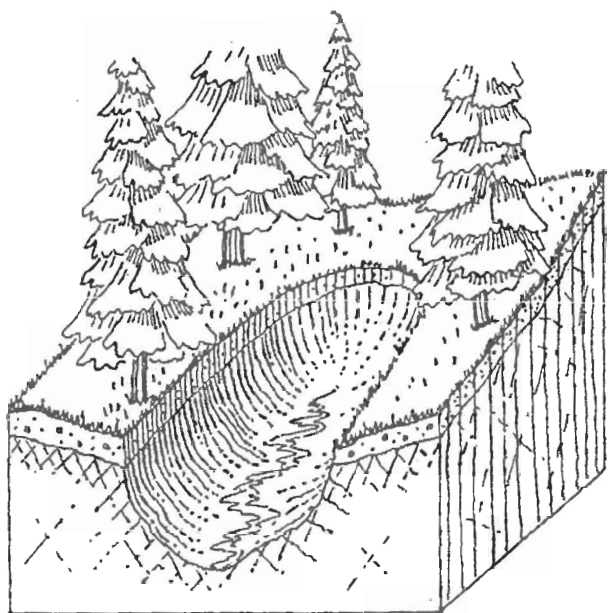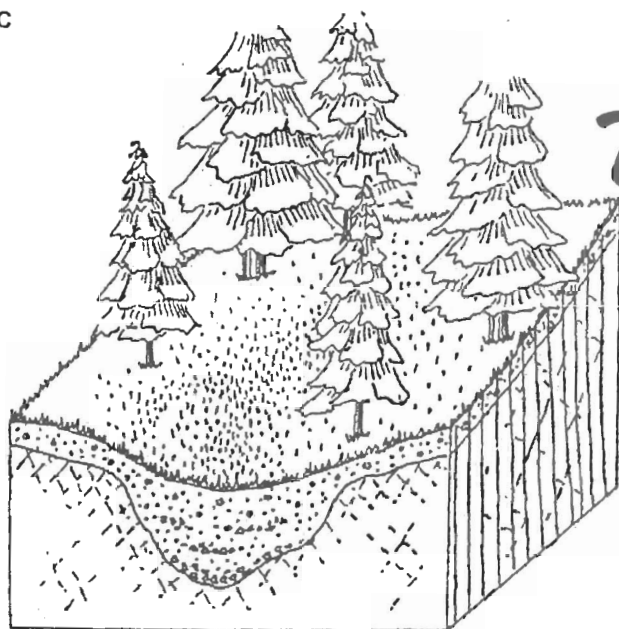
B
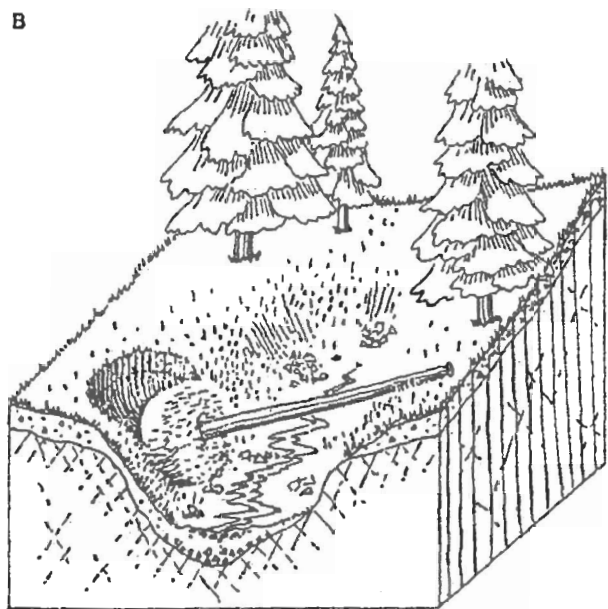
Figure 5—Evolution from a landslide scar in a bedrock depression to a soil wedge. After the landslide, the exposed bedorck surface forms an impermeable horizon shedding rainwater and subsurface discharge into the depression as overland flow. B. Sediment eroded from the over-steepened soil perimeter into the depression is washed of its fine component, leaving a gravel-lag deposit covering the rock surface. C. Continued deposition leads to less frequent saturation overland flow and less surface transport. Eventually, the lack of surface wash causes the soil near the surface of the soil wedge to become similar in texture to surrounding soil from which it is derived.

24

Driving Elements
e.g., gravity, water
pressure, seismic
shaking, windthrow

Resisting Elements
e.g., frictional resistance,
cohesion, root strength
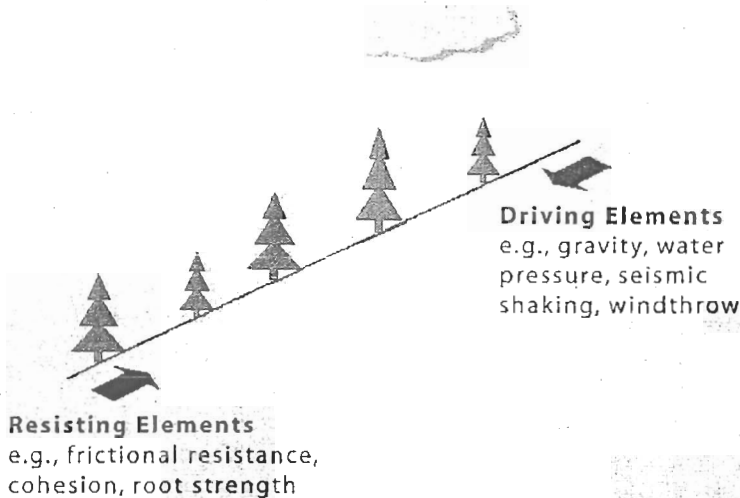
Figure 10. Schematic of a slope, showing driving and resisting elements.

and Wieczorek, 1995; Wilson, 1997; Wiley, 2000). Several of these studies have focused specifically on identifying rainfall thresholds above which landslides (and particularly debris flows) become significantly more widespread and numerous (Keefer and others, 1987; Wilson and Wieczorek, 1995; Wilson, 1997; Wiley, 2000).

One rainfall threshold study that used storm data specifically from the Pacific Northwest was reported by Wiley (2000). This study included evaluations of climatic data in comparison with landslide occurrences recorded for the period of February 1996 through January 1997 and indicated that widespread landslide activity in steep terrain throughout western Oregon is likely to be triggered by rainfall intensity/duration combinations of (a) 40

focused on evaluating relationships between storm characteristics and debris flow occurrences (e.g., Campbell, 1975; Crozier and Eyles, 1980; Keefer and others, 1987; Cannon, 1988; Wieczorek and Sarmiento, 1988; Wilson

↑N
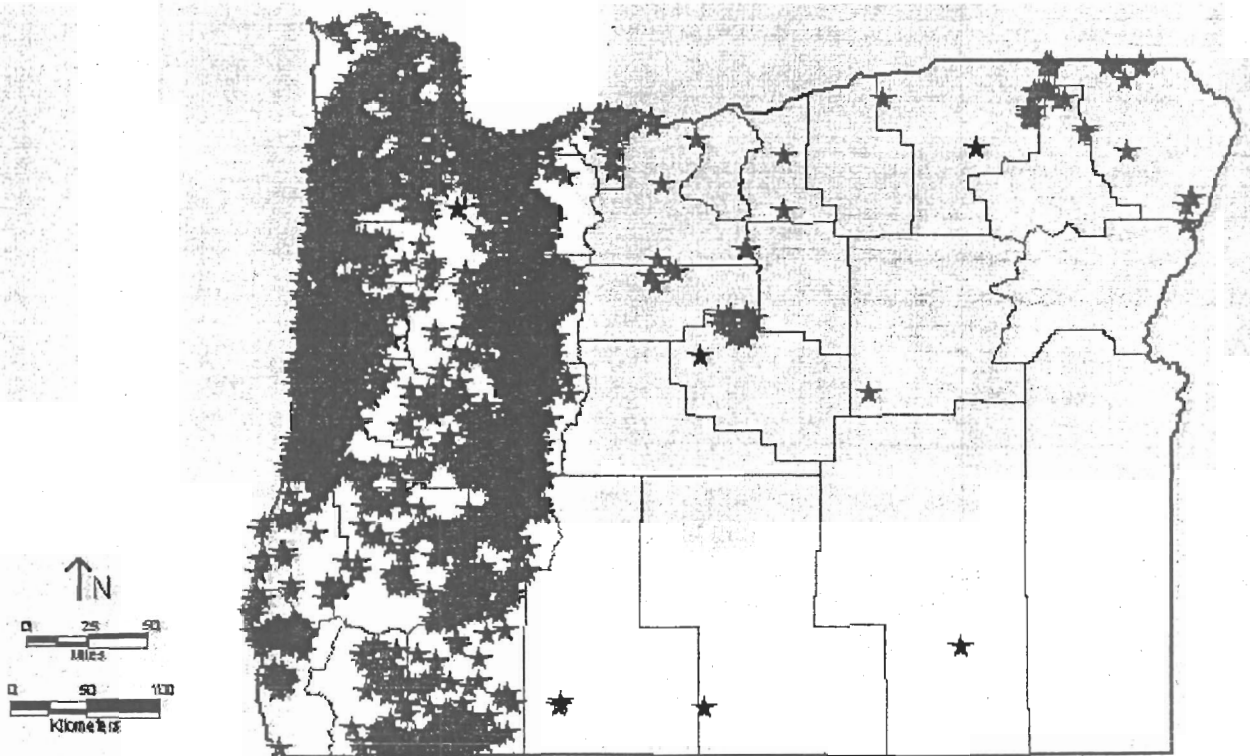
Figure 11. Distribution of the more than 9,500 landslides triggered in Oregon by the storms of 1996-97. (From Hofmeister, 2000)

41

interval greater than 100 years while the peak flow on the Wilson River (the next major river basin to the south) corresponded with a 25 year recurrence interval flood (Laenen et al., 1997). In the Oregon Cascades, peak flow on the Sandy River near Marmot corresponded with a recurrence interval greater than a 100 year flood while the nearby Hood River experienced a 10-15 year flood (Laenen et al., 1997).

November Storm

The November 1996 storm was a shorter duration and higher intensity rainfall event than the February storm. Since the November 1996 storm occurred early in the season, predominately at lower elevations in Oregon's Willamette Valley and southern Coast Range, it lacked a rain-on-snow component. Since it occurred in the fall it also lacked significant antecedent precipitation. Therefore, soil moisture levels prior to the storm event were relatively low. However, all-time, one-day precipitation records were set at many locations (Table 1).

In addition, the following comments by George Taylor (State Climatologist) characterize the storm:

"Daily and monthly records were set at many sites as well. At Portland Airport, 3.86 inches was recorded between 4 p.m. on the 18th and 4 p.m. on the 19th. This broke the November 24-hour total of 2.82 inches, which was set November 10-11, 1995. Rainfall intensities for some areas in the Willamette Valley and Coast Range were calculated as a 100-year return period. While rainfall amounts were high as were stream flows throughout the Willamette Valley, highest impacts in terms of landslides and debris flows were reported in Douglas and Coos counties."

Table 1. One-day precipitation records for selected stations.

Location	1996 Amount (in.)	Date Records Began	Old Record	Year Old Record Set (in.)
Corvallis	4.45	1889	4.28	1965
North Bend	6.67	1931	5.60	1981
Portland	2.70	1939	2.48	1948
Redmond	2.38	1948	1.81	1969
Roseburg	4.35	1931	3.28	1965

There is tremendous spatial variability in timing and intensity of rainfall events for any given storm. For example, two gages in the Oregon Coast were compared to determine if two gages recorded similar precipitation intensities during the same rainfall events (Surfleet, 1997). The two gages were at a similar elevation, a similar distance from coast and within 10 miles from each other. The two gages recorded markedly different storm intensities during significant rainfall events from 1989-1995. The precipitation timing and intensities were disparate enough to suggest that for the highest storm events at one gage the nearby gage was not experiencing a storm event. For example, 31 of the 33 top storms at one gage were not identifiable as one of the top ten storms at the second gage. The combination of variation in storm characteristics (precipitation and flood levels) and

Table 8. General summary of landslides for core area portions of the eight study areas (core study **area** refers to that subset of each study area surveyed in which all stream channels were systematically checked for delivering landslides).

	Red zone Study Areas					Random Study Areas			All
	Elk	Scottsburg	Mapleton	Tillamook	Vida	Vernonia	Dallas	Estacada	
Core-study area (sq/mile)	6.5	7.2	8.3	4.5	7.1	3.4	3.1	5.5	45.8
Landslides									
Active Road	2	5	13	7	6	2	2	0	37
Old Road	5	6	1	5	0	1	2	0	20
Non-road	152	78	92	50	53	16	6	2	449
Total	159	89	106	62	59	19	10	2	506
Landslide Erosion									
Active Road (yd^3)	1261	11544	4243	31603	14892	1240	167	0	64951
Old Road (yd^3)	2434	7654	191	8877	0	25	35501	0	54683
Non-road (yd^3)	49898	43628	17442	34014	14357	868	8516	20	168743
Total (yd^3)	53593	62826	21876	74495	29249	2133	44184	20	288376
Landslide Densities									
Total Slides (per sq. mi.)	24.4	12.3	12.8	13.8	8.3	5.5	3.2	0.4	11.1
#Non-road slides (per sq.mi.)	23.3	10.8	11.1	11.1	7.4	4.7	1.9	0.4	9.8
Landslide Erosion Rate									
Non-road slides (yd^3/ac)	12.0	9.5	3.3	11.8	3.1	0.4	4.2	0.01	5.8
All slides (yd^3/ac)	12.8	13.6	4.1	25.9	6.4	1.0	22.0	0.01	9.9

Table 9. Landslides identified outside of the core study areas. Streams were not systematically surveyed for landslides in these areas. This table shows only those landslides that directly influenced channels in the core areas.

Landslide Category	Redzone Study Areas					Random Study Areas			Total
	Elk	Scottsburg	Mapleton	Tillamook	Vida	Vernonia	Dallas	Estacada	All Sites
Channel Delivering Landslides									
Active Road	NA	NA	0	3	18	0	0	NA	21
Old Road	NA	NA	0	2	1	1	0	NA	4
Non-road	NA	NA	3	5	14	0	5	NA	27
Total	NA	NA	3	10	33	1	5	NA	52

Table 10. Characteristics of landslides within the core study areas.

	Red zone Study Areas					Random Study Areas			Total
Landslide Density	Elk	Scotts-burg	Mapleton	Tillamook	Vida	Vernonia	Dallas	Estacada	All Sites
# Non-road related Slides	152	78	92	50	53	16	6	2	449
Area surveyed (sq. mi)	6.52	7.21	8.29	4.49	7.14	3.44	3.14	5.49	45.7
#Non-road slides (per sq.mi.)	23.3	10.8	11.1	11.1	7.4	4.7	1.9	0.4	9.8*
Landslide Characteristics									Average
Average Width (ft)	22.3	29.7	15.1	36.4	18.1	23.0	62.0	13.0	24.0
Average Length (ft)	34.6	44.6	24.5	30.6	32.2	24.9	44.2	21.5	43.1
Average Area (acres)	0.020	0.035	0.010	0.046	0.015	0.015	0.076	0.006	0.023
Average Depth (ft)	1.9	3.3	2.1	2.4	2.7	2.1	2.9	0.6	2.5
Maximum Depth (ft)	3.5	5.5	3.6	4.5	4.6	3.9	5.0	2.3	4.3
Landslide Average Volume (yd^3)	58	216	26	274	74	49	340	5	109
Average Total Volume (including debris flow) (yd^3)	328	559	190	680	271	54	1419	10	376
Erosion (yd^3/acre.)	12.0	9.5	3.3	11.8	3.1	0.4	4.2	0.01	5.8

*Average

Robison, et al., 1999

1996 storm event

28

Table 11. Landslide occurrence by origin of occurrence and by study area geology.

Origin	Slides (No.)	Avg. Slope Blw. L.S. (%)	Depth Avg. (ft)	Initial L.S. Avg. Vol. (cu. yd.)	Initial L.S. Med. Vol. (cu. yd.)	Total L.S.* Avg. Vol. (cu. yd.)	Total L.S.* Med. Vol. (cu. yd.)
				Landslide Characteristics			
Red zone Tyee Sandstone Geology Study Areas (Elk Cr., Mapleton Scottsburg)							
Up-slope	239	82	2.5	104	36	446	174
Channel Adj.	82	91	1.9	41	46	55	17
Gully	1	55	0	0	0	4	4
Red zone Igneous Geology Study Areas (Tillamook, Vida)							
Up-slope	50	86	2.9	116	25	702	171
Channel Adj.	51	92	3.2	231	53	253	53
Gully	2	56	0	0	0	163	163
Stratified randomly Selected Study Sites (Dallas, Estacada, Vernonia)							
Up-slope	6	78	2.9	341	82	1434	142
Channel Adj.	18	93	2	44	17	44	17
Gully	0	NA	NA	NA	NA	NA	NA
All Study Sites							
Up-slope	295	83	2.5	111	36	509	171
Channel Adj.	151	92	2.3	105	24	120	25
Gully	3	56	0	0	0	110	61

The channel **adjacent** landslides occurred on steeper slopes than did the up-slope landslides (92% versus 83% steepness). Steepness is measured as rise (vertical distance) over run (horizontal distance) from the top of the landslide scarp downslope over the "reconstructed" (prior to the landslide) ground surface. Field crews were careful to try to measure slope on the initial landslide surface, based on the landslide depth measurements. Failure to do this can lead to overestimation of the pre-landslide slope steepness (which is a critical parameter for determination of landslide hazard). Note that slope percent and slope degrees are very different. A slope of 100% is equal to 45 degrees. The up-slope landslides originated on average slopes of 82% in the Tyee red zone study areas, 86% on the igneous red zone study areas, and 78% on the non red zone study areas; however, there were only six up-slope landslides in the stratified random study areas. Average slope steepness for the channel adjacent landslides was similar across all study zone types (91% to 93%).

Initial median landslide volumes for the Tyee and igneous study areas are similar (up-slope volume of 36 yards in the Tyee and 25 yards in the igneous, with channel adjacent volume of 46 and 53 cubic yards respectively). However, mean initial volumes are very different. In the Tyee study areas, up-slope landslides averaged 104 cubic yards while channel adjacent landslides averaged 41 cubic yards. In the red zone igneous study areas, the channel adjacent landslides were larger than the up-slope landslides (231 cubic yards compared to 116 cubic yards). However, after including debris flow volumes, up-slope